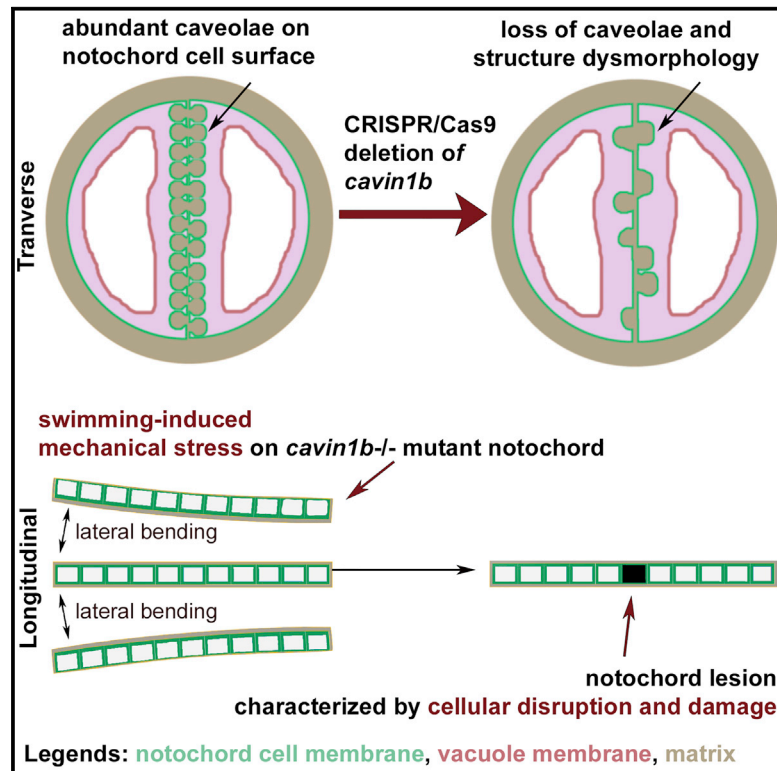


Current Biology

Caveolae Protect Notochord Cells against Catastrophic Mechanical Failure during Development

Graphical Abstract



Authors

Ye-Wheen Lim, Harriet P. Lo, Charles Ferguson, ..., Alpha S. Yap, Thomas E. Hall, Robert G. Parton

Correspondence

thomas.hall@imb.uq.edu.au (T.E.H.), r.parton@imb.uq.edu.au (R.G.P.)

In Brief

The notochord cell membrane is characterized by an abundance of caveolae. Lim et al. show that caveolae and Cavin1b, a coat protein required for notochord caveola formation, mediate embryonic notochord cell fragility during zebrafish early locomotion. These findings suggest a role for caveolae in conveying notochord cell mechanoprotection.

Highlights

- Zebrafish Cavin1b deletion induces notochord lesions and locomotor defects
- Notochord lesions are damaged and membrane-permeable cells
- The remaining *cavin1b* mutant caveolae are morphologically dysmorphic
- Mechanical stress leads to *cavin1b* mutant notochord cell collapse

Caveolae Protect Notochord Cells against Catastrophic Mechanical Failure during Development

Ye-Wheen Lim,¹ Harriet P. Lo,¹ Charles Ferguson,^{1,2} Nick Martel,¹ Jean Giacomotto,^{3,4} Guillermo A. Gomez,^{1,5} Alpha S. Yap,¹ Thomas E. Hall,^{1,*} and Robert G. Parton^{1,2,6,*}

¹Institute for Molecular Bioscience

²Centre for Microscopy and Microanalysis

The University of Queensland, Brisbane, QLD 4072, Australia

³Queensland Brain Institute, The University of Queensland, Brisbane, QLD 4072, Australia

⁴Institut NeuroMyoGene, CNRS UMR5310, INSERM U1217, Université Claude Bernard Lyon 1, 69622 Villeurbanne, France

⁵Centre for Cancer Biology, SA Pathology and the University of South Australia, Adelaide, SA 5000, Australia

⁶Lead Contact

*Correspondence: thomas.hall@imb.uq.edu.au (T.E.H.), r.parton@imb.uq.edu.au (R.G.P.)

<http://dx.doi.org/10.1016/j.cub.2017.05.067>

SUMMARY

The embryonic notochord is a flexible structure present during development that serves as scaffold for formation of the vertebrate spine. This rod-like organ is thought to have evolved in non-vertebrate chordates to facilitate locomotion by providing a rigid but flexible midline structure against which the axial muscles can contract. This hydrostatic “skeleton” is exposed to a variety of mechanical forces during oscillation of the body. There is evidence that caveolae, submicroscopic cup-shaped plasma membrane pits, can buffer tension in cells that undergo high levels of mechanical stress. Indeed, caveolae are particularly abundant in the embryonic notochord. In this study, we used the CRISPR/Cas9 system to generate a mutant zebrafish line lacking Cavin1b, a coat protein required for caveola formation. Our *cavin1b*^{-/-} zebrafish line exhibits reduced locomotor capacity and prominent notochord lesions characterized by necrotic, damaged, and membrane-permeable cells. Notochord diameter and body length are reduced, but remarkably, the mutants recover and are homozygous viable. By manipulating mechanical stress using a number of different assays, we show that progression of lesion severity in the mutant notochord is directly dependent on locomotion. We also demonstrate changes in caveola morphology in vivo in response to mechanical stress. Finally, induction of a catastrophic collapse of live *cavin1b*^{-/-} mutant notochord cells provides the first real-time observation of caveolae mediating cellular mechanoprotection.

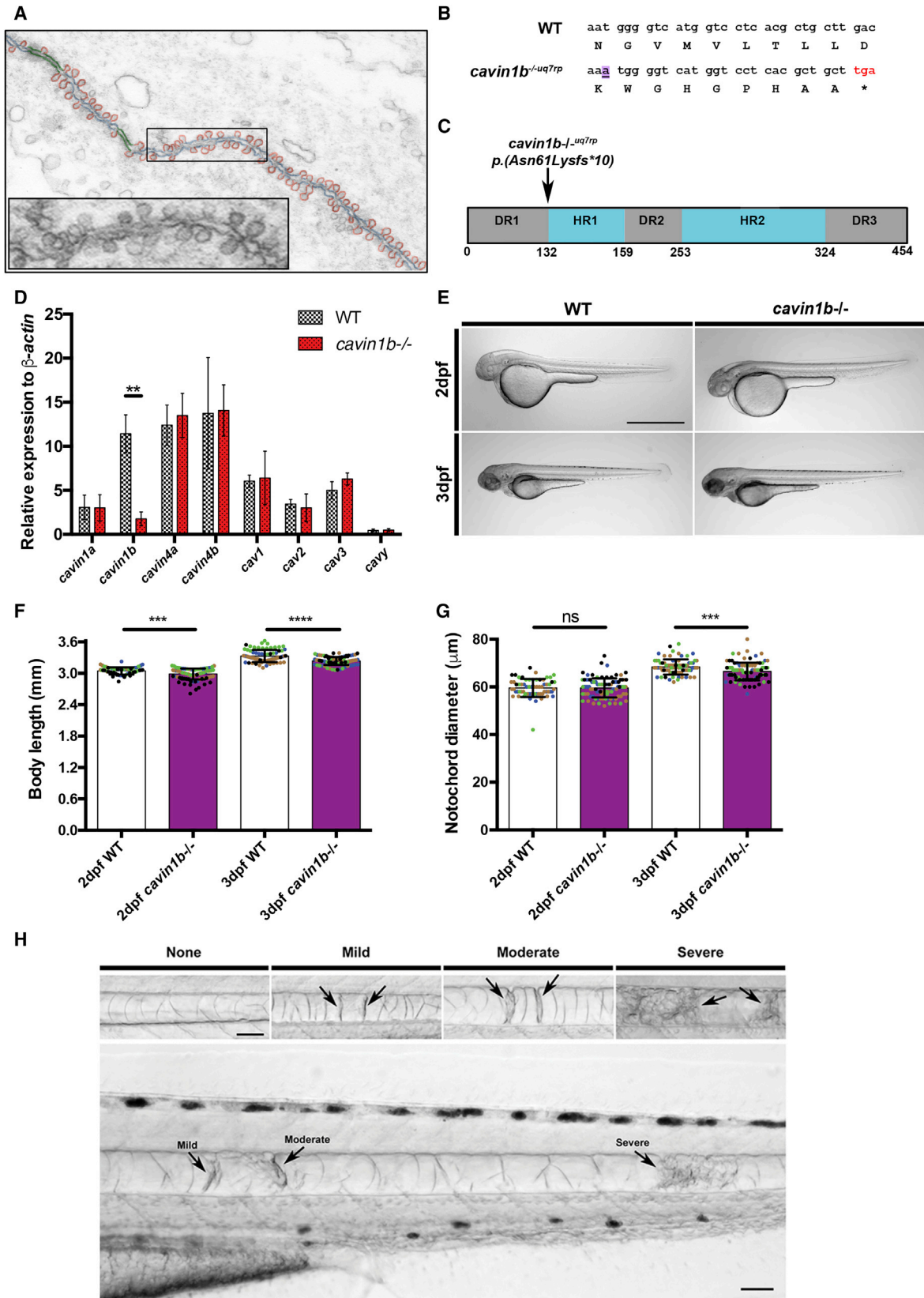
INTRODUCTION

The notochord is the defining feature of chordates. It plays a crucial structural role in embryonic development (reviewed by

Stemple [1]), acting as a hydrostatic skeleton to facilitate locomotion. Inner notochord cells are almost entirely filled with osmolyte-enriched large vacuoles, shown to be specialized lysosomes [2]. These cells are surrounded by outer sheath cells that secrete matrix to form the extracellular perinotochordal sheath [3]. The combination of hydrostatic pressure generated within notochord cell vacuoles and the surrounding sheath provides rigidity to the notochord and axial support to the entire embryo [4, 5]. This is critical for embryos of non-amniote chordates, such as fish, that develop externally and therefore must feed and evade predators before spine ossification.

One of the most striking features of the notochord in the zebrafish is the incredible density of caveolae, cell surface pits of approximately 65 nm diameter (Figure 1A). Caveolae are so densely packed in the central septa of the notochord, formed by the close apposition of neighboring notochord cells, that they increase the local surface area almost 2-fold [7]. The appearance of abundant caveolae occurs at ~30 hpf (hours post-fertilization), around the same time notochord cell vacuoles become fully differentiated, and this correlates with expression of the caveolar coat protein, Cavin1b [7, 8]. Two other caveola structural proteins are also expressed in the notochord, Caveolin1 (Cav1) and Caveolin3 (Cav3), and like Cavin1b, both are required for caveola formation [7, 9]. However, Cav1 expression occurs prior to caveola formation and it has been suggested that Cavin1b is switched on at this specific developmental stage to cause the massive increase in notochord caveola density [8]. The mammalian notochord also shows enrichment of CAV1 indicative of an evolutionary-conserved role in the notochord [10]. Caveolae have been shown to play a mechanoprotective role in muscle [11] and endothelial cells [12] in vivo. This suggests that caveolae may play a comparable role in the notochord.

Here, we have ablated *cavin1b* expression using genome-editing technology to examine its effect on notochord function during development. We now show that notochord caveola loss causes instability in specific regions of the notochord, characterized by cell death and formation of characteristic “lesions”. This causes shortening of the embryo through contraction along the body axis. Lesion formation in the knockout embryos correlates with locomotion, revealing a conserved role for notochord



(legend on next page)

caveolae in the mechanical strength and physical stability of the early embryo.

RESULTS

Cavin1b Loss Leads to Notochord Lesion Occurrence in the Developing Zebrafish

In view of the role of *cavin1b* in forming notochord caveolae, we used the CRISPR/Cas9 system to generate a stable knockout zebrafish line. Several stable *f1* heterozygotes possessing *cavin1b* mutant alleles were identified, from which a single line (*cavin1b*^{-l-uq7rp}, hereafter referred to as *cavin1b*^{-/-}) was selected and bred to homozygosity (Figures S1A–S1D). This mutant line possesses a frameshift mutation and predicted truncation of the Cavin1b protein, removing highly conserved helical regions crucial to cavin function (Figures 1B and 1C) [13]. RT-PCR and qRT-PCR of *cavin1b* mRNA revealed reduced levels relative to wild-type (WT), suggesting nonsense-mediated decay [14] (Figures S1F and 1D; qRT-PCR primers in Table S1).

We were able to maintain *cavin1b*^{-/-} lines through several generations, demonstrating that *cavin1b*^{-/-} mutants are viable and fertile. However, we observed a lower than expected ratio of homozygotes to heterozygotes compared to expected Mendelian ratios (47.73% heterozygotes, 38.63% WT, and 13.63% homozygotes compared to 50%, 25%, and 25%; Figure S1E). This suggests a lower survival rate of *cavin1b*^{-/-} homozygotes in comparison to WT and heterozygotes. Initial observations of embryonic morphology showed no gross differences between *cavin1b*^{-/-} zebrafish and WT (Figure 1E). However, morphometric analyses revealed that *cavin1b*^{-/-} embryos possessed a significantly shorter body length compared to WT at 2 and 3 dpf (days post-fertilization) (Figure 1F) and a significant reduction in notochord diameter at 3 dpf (Figure 1G). Most notably, however, beginning at the 48-hpf stage, intranotochordal lesions were frequently visible in mutant embryos (Figures 1H and 2A).

From the end of the segmentation stage (~20 hpf), the notochord differentiates from the chordamesoderm [15, 16]. To inspect lesion appearance, we examined this developmental

transition using the vital dye BODIPY FL C5-Ceramide, which labels the plasma membrane. We observed normal pre-vacuolation notochord morphology (Figure S2A) and normal post-inflation vacuole morphology (Figures S2B–S2F). Time course observations revealed that lesions emerged in differentiated notochords and became progressively more severe over the course of 20 hr (Figure 2A). We classified notochord lesions according to their severity: mild; moderate; or severe (Figure 1H). Mild lesions were those that were partially delaminated between apposing notochord cells; moderate lesions showed a larger delamination and tended to be flanked by fragmented vacuoles, whereas severe lesions showed high contrast under differential interference contrast (DIC), accumulating dense material labeled with BODIPY FL C5-Ceramide (plasma membrane) and BODIPY TR methyl ester (endomembranes; Figure 2B). Fragmented vacuoles occurred only within lesion sites. These lesions were also characterized by F-actin accumulation, with no significant changes in actin cortex distribution in non-lesion sites (Figures S3A–S3D).

Quantification of notochord lesion severity within embryo populations revealed an increase in the moderate lesion proportion and the emergence of severe lesions as *cavin1b*^{-/-} embryos matured from 2 to 3 dpf (Figure 2C). Individual *cavin1b*^{-/-} embryos were also given a total severity index score, which reflected both lesion number and severity. Both lesion number and severity score were observed to increase as *cavin1b*^{-/-} embryos matured from 2 to 3 dpf (Figures 2D and S6A). These lesions persisted up to at least 12 dpf before whole vertebra formation (Figure 2E). We also observed a significantly shorter body length in 15-dpf *cavin1b*^{-/-} larvae compared to WT (Figure 2F), indicating a continuing defect in anterior-posterior axis elongation, even though vertebra segmentation and formation were unaffected (Figures S3I and S3J). *Cavin1b* loss corresponds to the stochastic emergence of notochord lesions, which correlates with a decrease in notochord diameter and body length from 3 dpf onward. Similar lesion morphology was also observed in a second CRISPR/Cas9 generated *cavin1b* allele (*cavin1b*^{-l-uqrp8}), indicating that this phenotype is specifically associated with *cavin1b* loss (Figures S1G and S1H).

Figure 1. Mutant *cavin1b*^{-/-} Zebrafish Exhibit Notochord Lesions

(A) Electron micrograph depicting dense caveolae in the septum between two neighboring zebrafish embryonic notochord cells. Superimposed schematic trace highlights abundant caveolae (red), plasma membrane (blue), and junctions (green). The inset shows magnification of highlighted area.

(B) Alignment of nucleotide and deduced amino acid sequences from WT and *cavin1b*^{-/-} lines. An adenine insertion in the mutant sequence is highlighted in purple and underlined. Asterisk (*) indicates the truncating stop codon in the mutant sequence (marked in red). See Figures S1A–S1E for *cavin1b* CRISPR/Cas9 mutant generation and genotyping.

(C) Cavin1b protein domains (schematic). Arrow indicates the site of predicted truncation of selected mutant. The DR (disordered region) and HR (helical region) protein regions are boxed in gray and blue, respectively. Standard sequence mutation nomenclature is used [6].

(D) mRNA expression levels of caveola-associated genes by qRT-PCR (relative to β -actin). 5-dpf WT and *cavin1b*^{-/-} embryos are shown (n = 3 clutches; performed in triplicate). See Figure S1F for related RT-PCR gel. **p \leq 0.01; two-way ANOVA with Tukey's multiple-comparison test. Data are presented as mean \pm SD. See Table S1 for primer details.

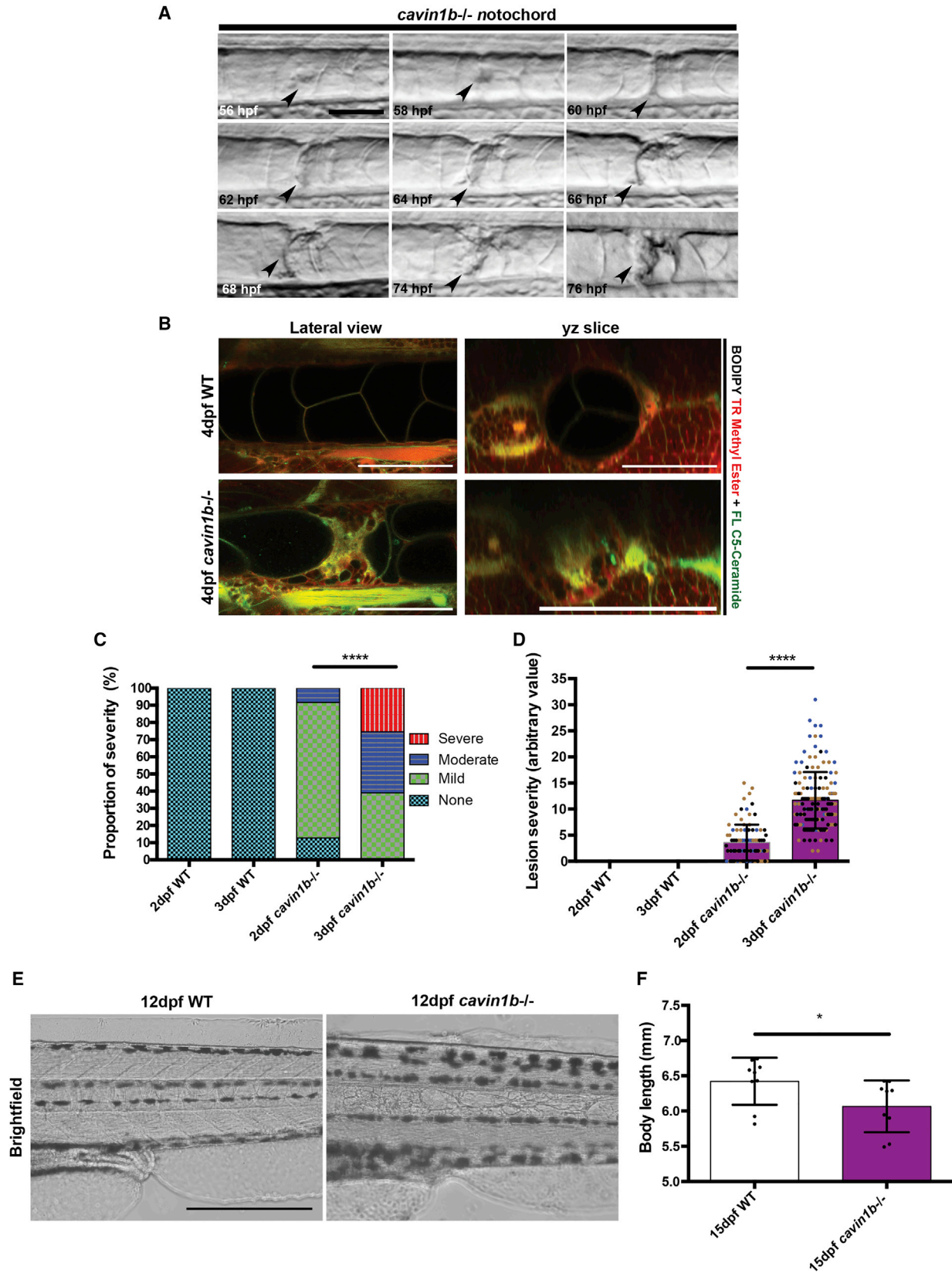
(E) Gross morphology of live 2- and 3-dpf WT and *cavin1b*^{-/-} embryos (treated with 1-phenyl-2-thiourea [PTU] to inhibit melanization). The scale bar represents 1 mm.

(F) Body length (mm) in 2- and 3-dpf WT and *cavin1b*^{-/-} embryos (2 dpf: n = 62 [WT] and n = 93 [mutant]; 3 dpf: n = 76 [WT] and n = 100 [mutant]). Four clutches per group are shown. Colored dots indicate different clutches.

(G) Notochord diameter (μ m) of 2- and 3-dpf WT and *cavin1b*^{-/-} embryos (2 dpf: n = 65 [WT] and n = 94 [mutant]; 3 dpf: n = 79 [WT] and n = 100 [mutant]). Four clutches per group are shown. For observations on live chordamesoderm transition, see Figure S2A. For characterization of notochord vacuole formation, see Figures S2B–S2F.

For (F)–(G), ns, p > 0.05; ***p \leq 0.001; ****p \leq 0.0001; two-tailed t tests. Data are presented as mean \pm SD.

(H) Notochord lesions. (Top row) Notochord lesions of varying severity (mild, moderate, or severe) are shown. (Bottom row) Representative image of a 3-dpf *cavin1b*^{-/-} notochord possessing all three qualities of lesion severity is shown. The scale bar represents 50 μ m. See Figures S1G and S1H for lesions in another *cavin1b* mutant line.



(legend on next page)

Cavin1b^{-/-} Notochord Lesions Represent Damaged and Permeable Cells

Evans Blue Dye (EBD) is used as an intravital dye to assess in vivo membrane permeability and cell damage in mice and zebrafish [17, 18]. EBD uptake was observed in *cavin1b^{-/-}* embryos in mild lesion sites, with no uptake in neighboring notochord cells (Figure 3A). Using the same principle of dye uptake, we also utilized green fluorescent Alexa 488 5-UTP [19, 20]. Confocal images of moderate and severe lesions showed uptake of Alexa 488 5-UTP, with no uptake in undamaged neighboring cells labeled with BODIPY TR methyl ester (Figure 3B). These results demonstrate that all observable lesions of differing severity show prominent plasma membrane permeability, indicating compromised integrity.

Cavin1b^{-/-} Notochords Show Reduced Caveola Density, Abnormal Caveola Morphology, and Necrotic Cells

We next carried out detailed ultrastructural analyses of notochord morphology in 3- and 6-dpf *cavin1b^{-/-}* embryos and WT controls. *Cavin1b^{-/-}* embryos showed a marked loss of notochord caveolae at all stages examined, in comparison to WT (Figures 4A–4F, 5A–5C, 5G, and 5H), and in contrast to sarcolemmal caveolae, where we detected no morphology and density differences (Figure S4E). 3-dpf quantitation revealed a greater than 3-fold decrease in caveola density in *cavin1b^{-/-}* notochord cells (Figure S4A). Remarkably, the remaining caveolae showed a dramatic change in morphology. Rather than the characteristic bulb shape with a narrow neck observed in WT notochords (Figure 4C; see representative caveola in Figure S4C), *cavin1b^{-/-}* notochord caveolae were noticeably widened, with a wide neck, and were shallow in depth (Figure 4F; see representative caveola in Figure S4D). This was quantified using the ratio of caveola neck diameter to depth. In WT notochords, the neck:depth ratio was <1, indicating a relatively narrow neck as compared to the depth of the caveola, whereas in *cavin1b^{-/-}* notochords, the neck:depth ratio was >1, indicating a relatively wide neck and shallow pit (Figure S4B). This implies that the remaining caveolae showed morphology change from a cup-shaped invagination to a more widened (dysmorphic) state upon *cavin1b* loss. Electron microscopy (EM) longitudinal sections in lesion-rich areas revealed highly aberrant *cavin1b^{-/-}* notochord cells correlating with local lesion densities observed by light microscopy (Figures 5D–5F and S4F). The notochord lesion site had a collapsed and necrotic appearance characterized by electron-dense cellular debris and generally disrupted morphology (Figure 5D). Altogether, these ultrastructural obser-

ations show that *cavin1b* loss perturbs both caveola number and morphology and causes notochord lesions where cells are disrupted and necrotic.

Cavin1b^{-/-} Notochord Lesion Severity and Number Depends on Mechanical Stress

Using a laser ablation technique, we showed that the underlying cortical tension in live *cavin1b^{-/-}* notochord cells (represented by initial recoil after membrane ablation) has a modest but significant reduction, given a similar K value (ratio of junctional elasticity to viscosity of media; Figures S3E–S3H) [21]. We noted that, although all *cavin1b^{-/-}* notochord cells showed a similar reduction in caveola density, intravital dye uptake only occurred within lesions. These data suggested that external factors might cause cellular damage at specific sites. The notochord acts as an axial support during swimming and can be posited as a structural skeleton for muscle antagonism and restriction of undulatory bending [22, 23]. We therefore hypothesized that mechanical stress as the embryo swims might be particularly pronounced in specific regions along the length of the notochord, driving cellular damage. To examine this, we mapped the position of lesions along the length of *cavin1b^{-/-}* embryos. Indeed, the notochord lesion position peaked in the posterior of the embryo, approximately between the anus and the tip of the tail (Figures 6A and 6B). This corresponds to the region of maximum flexion during swimming [23–25].

We next tested the hypothesis that mechanical stress causes cell disruption and lesion formation in *cavin1b^{-/-}* embryos. Swimming results in mechanical loading on the notochord by neighboring skeletal muscles [23, 26]. We developed methods to either increase or reduce swimming-induced mechanical stress on the notochord. We used a constant voltage electrical stimulator to generate muscle contraction on the notochord (80 s high-intensity stimulation) and immediately processed stimulated WT zebrafish for EM. Strikingly, we observed that stimulated neighboring notochord cells were less apposed and “scaloped” with contacts remaining at putative junctions (Figure S5A). The stimulated notochord ultrastructure was characterized by caveola density reduction, with some remaining caveola structures being dysmorphic (Figures S5B and S5D). Thus, we posit that WT notochord caveolae flattened in response to contraction-induced mechanical loading, suggesting a mechanism to prevent lesion formation. We next tested whether electrically stimulated muscle contraction on the *cavin1b^{-/-}* notochord correlates with lesion formation. We electrically stimulated embryos for 10 min and scored notochord

Figure 2. Notochord Lesions Manifest in Varying Severity and Number

- (A) Initiation of lesion formation in a live *cavin1b^{-/-}* embryo from 56 hpf to 76 hpf (arrowhead marks lesion). The scale bar represents 50 μ m.
- (B) Accumulation of intravital markers of plasma membrane (green, BODIPY FL C5-Ceramide) and endomembranes (red, BODIPY TR methyl ester). Live confocal images of 4-dpf WT and *cavin1b^{-/-}* notochords are shown. Lateral and transverse images are taken from the same z stack. The scale bar represents 100 μ m. For characterization of underlying actin cortex, including actin status in lesions and cortical tension, see Figures S3A–S3H.
- (C) Proportion of lesions classed as mild, moderate, or severe between 2 and 3 dpf in WT and *cavin1b^{-/-}* embryos. ****p \leq 0.0001; chi square test.
- (D) Progression of individual phenotypic severity between 2 and 3 dpf using the “severity index,” a function of lesion number and lesion severity in WT and *cavin1b^{-/-}* embryos. Colored dots indicate different clutches. ****p \leq 0.0001; two-tailed t test.
- For (C) and (D), 2 dpf: n = 62 (WT) and n = 72 (mutant); 3 dpf: n = 93 (WT) and n = 144 (mutant); three clutches per group. Data are presented as mean \pm SD. For number of lesions per fish, see Figure S6A.
- (E) Live images of late-stage (12 dpf) larval notochords. Note the irregular cellular morphology in *cavin1b^{-/-}* compared to WT. The scale bar represents 400 μ m.
- (F) Body length of 15-dpf WT and *cavin1b^{-/-}* larvae (n = 9; clutch = 2 each group). *p \leq 0.05; two-tailed t test. Data are presented as mean \pm SD. See Figures S3I and S3J for calcein staining of 15-dpf embryos.

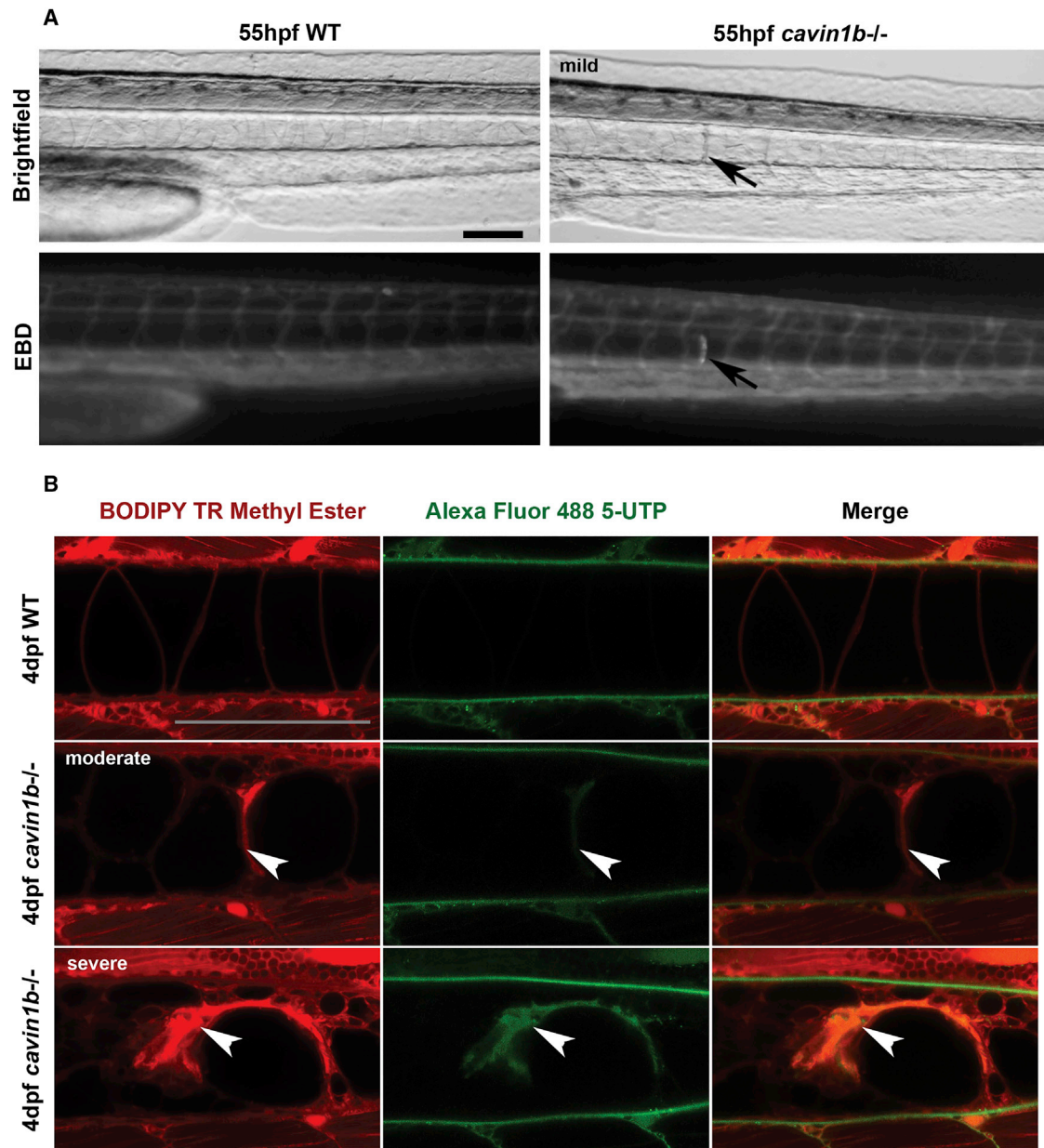


Figure 3. Notochord Lesions Are Damaged and Membrane-Permeable Cells

(A) Evans Blue Dye (EBD) infiltration into membrane-compromised notochord cells in live 55-hpf embryos. Arrows mark the mild lesion with corresponding specific EBD uptake. Note no uptake in skeletal muscles. Four fish per group are shown. The scale bar represents 100 μm.

(B) Alexa 488 5-UTP infiltration into membrane-compromised notochord cells in live 4-dpf embryos. Colocalization of Alexa 488 5-UTP with BODIPY TR methyl ester (endomembranes) occurred in moderate (middle row) and severe lesions (bottom row). No uptake in skeletal muscles was observed. Arrowheads mark lesions. $n = 5$ (WT) and $n = 10$ (mutant). The scale bar represents 100 μm.

lesions 24 hr post-stimulation. Stimulated *cavin1b*^{-/-} embryos showed a higher number of severe lesions spanning almost the entire notochord compared to controls (Figures 6C and S6F). Notochord lesion number and severity were also significantly increased in comparison to unstimulated *cavin1b*^{-/-} embryos (Figures 6D, 6E, and S6G). In addition, the stimulated *cavin1b*^{-/-} notochord exhibited a significant caveola density reduction, suggesting flattening of some of the remaining dysmorphic caveolae (Figure S5C). An increase in lesion phenotype

was also observed when we subjected *cavin1b*^{-/-} embryos to increased flexion by bleaching the chorion of *cavin1b*^{-/-} embryos at 1 dpf. Whereas embryos would normally hatch at 3 dpf, bleaching prevented chorion rupture and the growing embryos experienced increased flexion until they are released with forceps (Figure S6B). *Cavin1b*^{-/-} embryos raised inside bleached chorions showed a significant increase in lesion number and severity compared to unbleached WT embryos (Figures S6C–S6E).

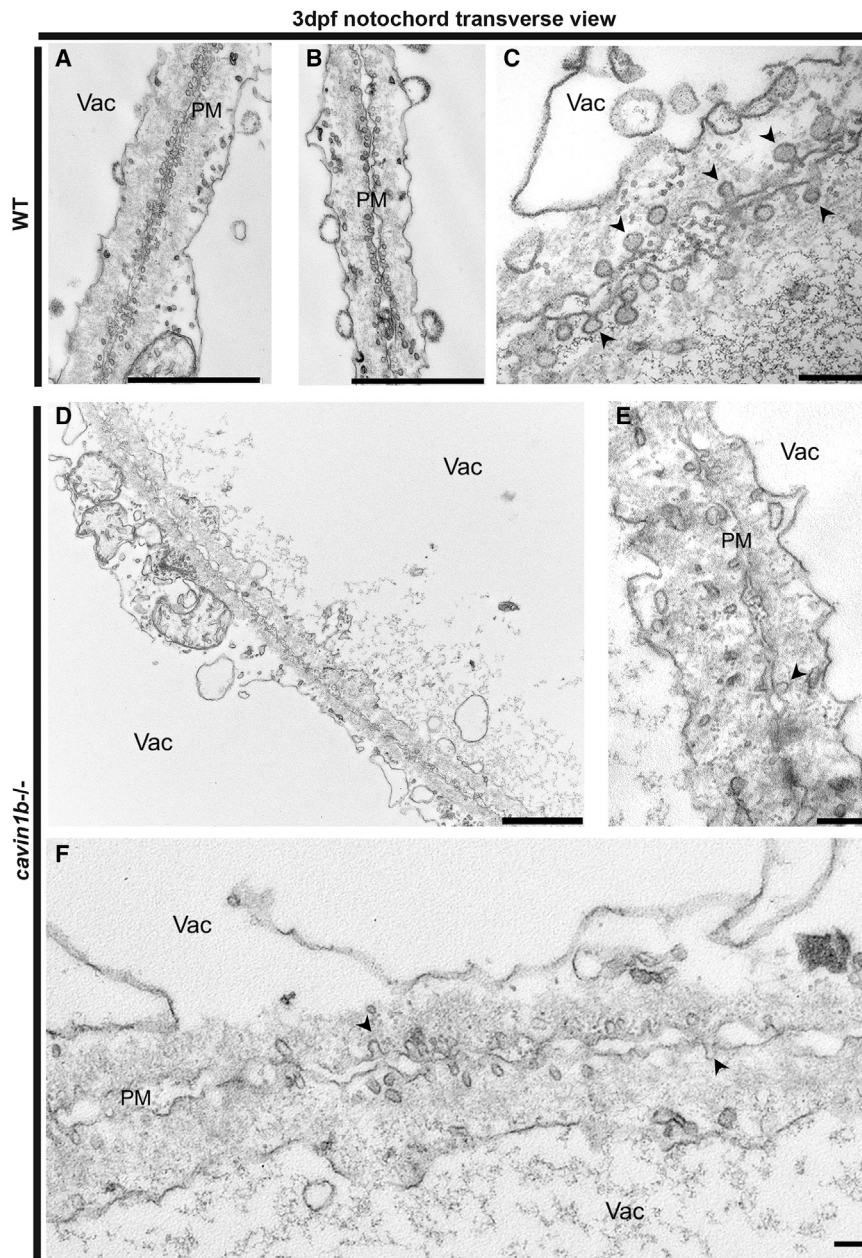


Figure 4. Transverse Ultrastructure of 3-dpf *cavin1b*^{-/-} Notochords

Ultrastructure of the junction between two neighboring notochord cells in non-lesion sites from WT (A–C) and *cavin1b*^{-/-} (D–F) zebrafish embryos. Higher magnification in (C) shows dense caveolae in the membranes of adjacent cells in WT. Higher magnification in (E) and (F) highlights loss of caveola density in the septa between *cavin1b*^{-/-} cells. Black arrowheads indicate caveolae. Note the differences in morphology between 3-dpf WT and *cavin1b*^{-/-} caveolae. For quantitation of caveola number and shape description, refer to [Figures S4A–S4D](#). PM, plasma membrane; Vac, vacuole. The scale bars represent (A, B, and D–F) 2 μ m and (C) 200 nm. For ultrastructure of skeletal muscle, refer to [Figure S4E](#).

also resulted in a significant increase in lesion severity and number occurring after a washout event ([Figures S7A and S7B](#)). Taken together, these data strongly suggest that *cavin1b* deletion renders notochords more sensitive to the mechanical stress of locomotion.

Real-Time Imaging Reveals Notochord Cell Collapse in Response to Mechanical Stress

The increased lesion formation in *cavin1b*^{-/-} embryos following electrical stimulation allowed us to investigate lesion progression in real time using live imaging. 3 dpf *cavin1b*^{-/-} embryos were subjected to prolonged electrical stimulation over a period of 40 min while under stereomicroscope recording. Some *cavin1b*^{-/-} notochord cells appeared to completely compress into lesion sites under prolonged contraction, which was associated with notochord area reduction ([Figures 7A and 7B](#)). We next used confocal microscopy to characterize the effects of prolonged electrical stimulation over a

We next tested whether a reduction in muscle activity would reduce lesion formation. For this, we utilized tricaine, an anesthetic that inhibits muscle activity by acting on voltage-gated sodium channels [27]. Notably, 3-dpf *cavin1b*^{-/-} embryos showed a significant reduction in lesion number after immobilization in anesthetic for 24 hr compared to unanesthetized 3-dpf embryos but a similar number of lesions to unanesthetized 2-dpf *cavin1b*^{-/-} embryos ([Figure 6G](#)). Progression of notochord lesion severity was significantly reduced in anesthetized *cavin1b*^{-/-} embryos after 24 hr compared to controls, but not halted ([Figures 6F and 6H](#)). Therefore, although lesion formation was temporarily arrested, progression of severity was reduced, but not abrogated. Tricaine removal at different time points

period of 76 min on a 65-hpf *cavin1b*^{-/-} embryo dual labeled with BODIPY FL C5-Ceramide and TR methyl ester. This time-lapse imaging revealed the catastrophic collapse of a notochord cell region in vivo ([Figures 7C and 7D](#); [Movie S1](#); control in [Figure S6H](#)). A schematic trace of the phenomenon revealed the collapse and compression of a single cell after approximately 40 min of stimulation (collapsing cell in purple, [Figure 7D](#)) and dramatic shape changes in neighboring cells (cells in yellow, [Figure 7D](#)) to accommodate for intercellular tension experienced following collapse. This is followed by a real-time observation of lesion severity progressing from moderate to severe and the de novo emergence of a new mild lesion (bottom row, [Figure 7D](#)).

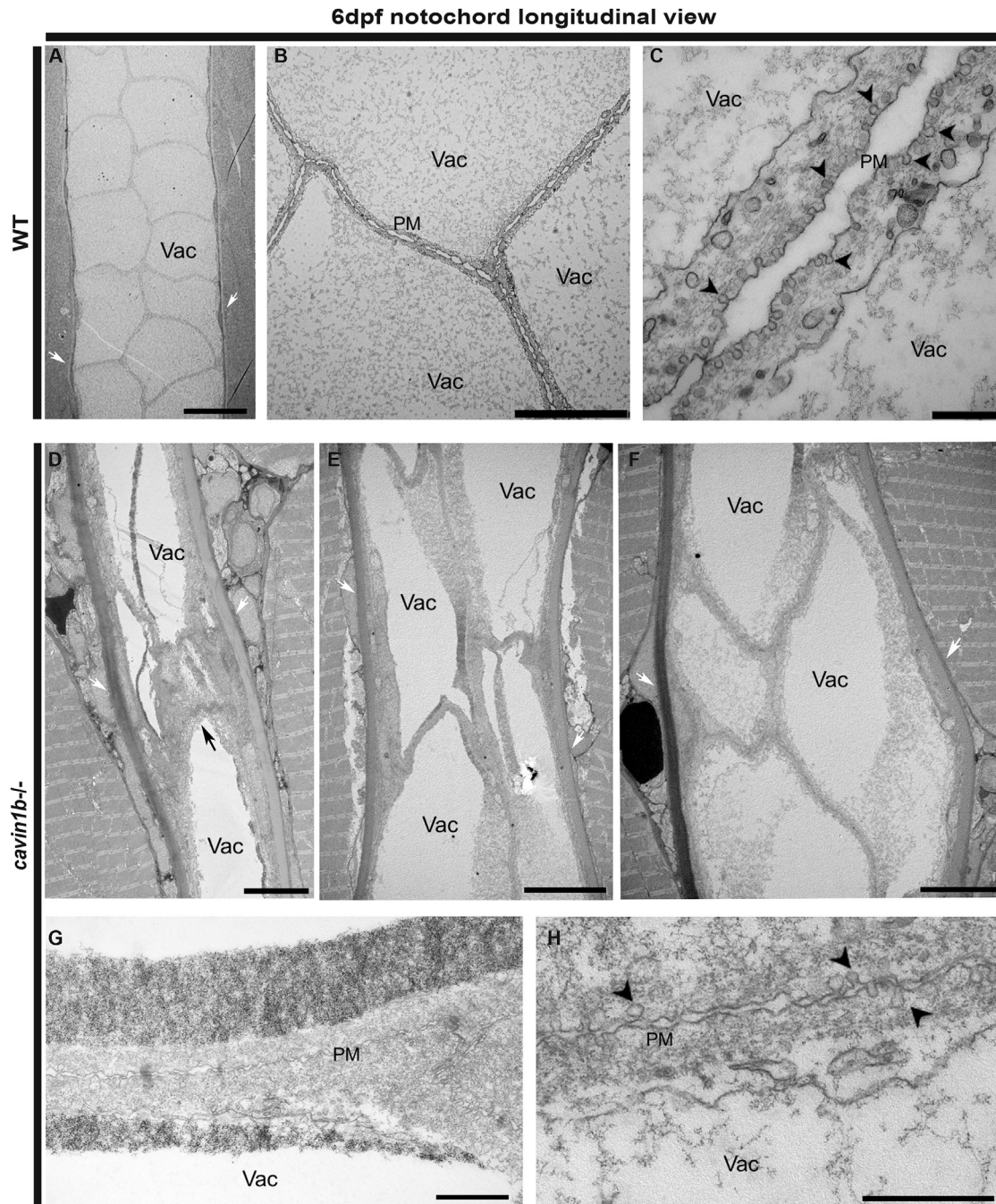


Figure 5. Longitudinal Ultrastructure of 6-dpf *cavin1b^{-/-}* Notochords

(A–C) Electron micrographs of a notochord longitudinal section from a 6-dpf WT embryo. Magnified view in (B) shows tightly apposed neighboring notochordal cells. (C) depicts neighboring notochord cells and caveolae.

(D–F) Longitudinal electron micrographs of notochord regions in lesion-rich sites from 6-dpf *cavin1b^{-/-}* embryos, each image representing a different zebrafish. Note aberrantly shaped vacuoles and disrupted cell morphology. For correlative light microscopy image of lesion presented in (D), refer to [Figure S4F](#).

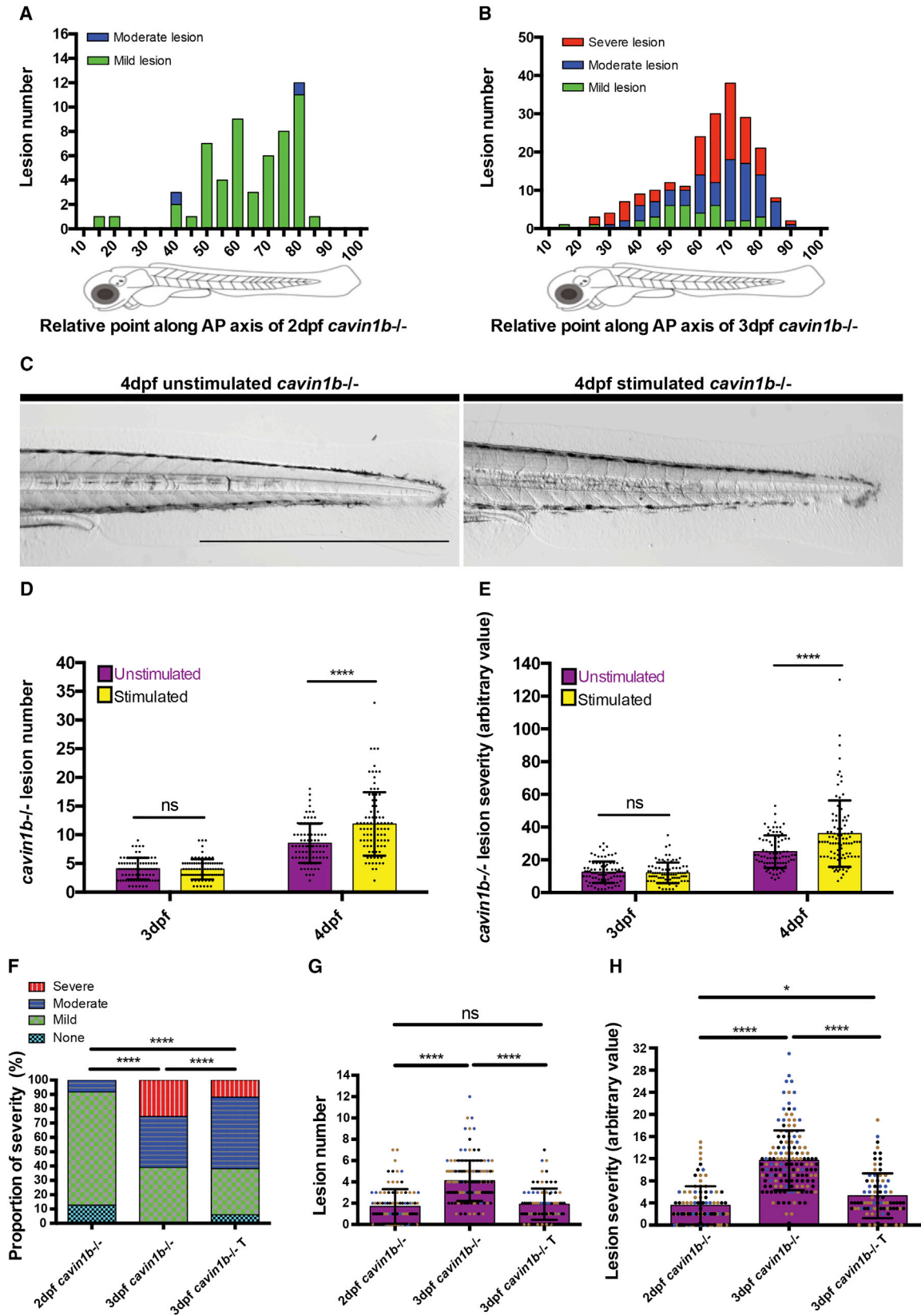
(G and H) Longitudinal electron micrographs of *cavin1b^{-/-}* cell-cell septum between notochord cells showing a prominent reduction in caveola number.

Black arrow, notochord lesion; black arrowhead, caveola; white arrow, perinotochordal sheath. The scale bars represent (A, B, and D–F) 10 μ m and (C, G, and H) 500 nm.

Cavin1b^{-/-} Zebrafish Early Larvae Exhibit Swimming Deficiencies

The embryonic notochord is hypothesized to function as a rigid structure, allowing muscle contraction to drive movement by

contracting against it [28, 29]. As such, *cavin1b^{-/-}* zebrafish should exhibit defects in early swimming performance. To this end, we measured swimming performance using an automatic tracking platform. We were able to measure decreased



(legend on next page)

swimming performances in *cavin1b*^{-/-} zebrafish. Specifically, at 5 and 6 dpf, *cavin1b*^{-/-} zebrafish traveled a significantly lower total distance over a 1-hr period of free swimming (Figures 7E–7G). A touch-evoked response assay also showed that 4- and 5-dpf *cavin1b*^{-/-} embryos traveled significantly shorter distances upon touch stimuli (Figures S7C and S7D). Overall, these experiments demonstrate that a reduction in notochord caveolae results in reduced early swimming function in *cavin1b*^{-/-} zebrafish, through the catastrophic loss of notochord cell integrity.

DISCUSSION

Cells are exposed to differing mechanical forces during development and homeostasis. The vertebrate notochord is a notable example where cells must compensate for constant and rapid changes in mechanical stress and tension [4, 5, 23]. Caveolae have been shown to buffer membrane tension in a number of model systems [11, 12, 30]. Indeed, the caveola density in notochord membranes is one of the highest ever recorded [7]. We have now shown that Cavin1b loss in the zebrafish notochord results in lesions generated through catastrophic membrane failure and cellular collapse. This, in turn, is followed by a reduction in body length and impaired early swimming function. By manipulating mechanical forces on the notochord using a variety of experimental paradigms, we have demonstrated that, under conditions of increased tension, the phenotype is exacerbated, and conversely, under reduced tension, the phenotype is suppressed.

Despite striking phenotypes displayed by *cavin1b*^{-/-} zebrafish, they are nonetheless able to recover locomotor capacity by 7 dpf. The notochord serves post-embryonically as the deposition site of segmented vertebral bodies at approximately 7 dpf [31–33]. These vertebral structures become increasingly important in managing lateral undulatory movements, substituting notochord roles during swimming [34]. Correct spine formation requires the presence of notochord cells and properly inflated notochord vacuoles [2, 31]. In *cavin1b*^{-/-} mutants, during chordacentrum formation, the vertebral column is still occupied by persistent residual cells. No focal bending or kinking was observed in the notochords of *cavin1b*^{-/-} larvae, which is a precursor of vertebral malformation [2, 35].

Caveola biogenesis and curvature requires cavin and caveolin protein expression [36]. Caveolin proteins can generate cur-

vature [37], but in mammalian cells, cavins are also required to generate the characteristic bulb-shaped morphology [8, 38]. We have shown that the stable knockout of Cavin1b, the Cavin1 paralog specific to the zebrafish notochord reduced but did not completely abolish caveola formation. This was unexpected because embryos were derived from a homozygous incross so there was no maternal contribution, and we found no evidence of upregulation of any other caveolar protein that might compensate. It remains formally possible, however, that low levels of another cavin protein, such as Cavin1a, might be present in levels undetectable by in situ hybridization [11]. It is notable that zebrafish Cavin1b is unusual when compared to mammalian Cavin1, in that it has five repeats of a specific conserved undecad (11-amino-acid) sequence rather than the canonical two, which we have previously speculated might effect caveola formation [36]. The remaining *cavin1b*^{-/-} notochord caveolae showed a dramatic change in morphology. Instead of the characteristic narrow neck and bulb shape of WT caveolae, *cavin1b*^{-/-} notochord caveolae were more variable in morphology and shallow without a clearly defined neck region. In electrically stimulated *cavin1b*^{-/-} zebrafish, we observed a reduction in the density of the remaining dysmorphic notochord caveolae. *Cavin1b*^{-/-} residual caveolae appeared to flatten in similar proportions to WT caveolae under similar stimulation conditions. Whether other membrane binding and remodeling proteins are involved in this process is not well understood. EHD2, for example, forms a ring at the neck of caveolae to control caveola budding [39–41], but the wide neck of *cavin1b*^{-/-} notochord caveolae would be unlikely to accommodate the EHD2 ring.

Even though we detected no changes in the actin cortex upon *cavin1b* loss (consistent with previous studies demonstrating that caveola flattening in response to hypotonic stress is an actin-independent process [30]), we measured a modest but significant reduction in live *cavin1b*^{-/-} notochord resting cortical tension, consistent with results from mammalian cells [30]. We hypothesize that the reduced caveola number and structural irregularities in *cavin1b*^{-/-} notochord cells contributed to this lowered membrane tension. Indeed, observations of the WT notochord membrane in response to mechanical stress showed widening and flattening of caveolae comparable to the default morphology of *cavin1b*^{-/-} notochord caveolae. This suggests that this membrane configuration might be linked

Figure 6. Notochord Lesion Formation and Severity Is Dependent on Locomotion

(A and B) Frequency of mild, moderate, and severe lesions along the anterior-posterior (AP) axis of 2-dpf (A) and 3-dpf (B) *cavin1b*^{-/-} embryos. No severe lesions were observed in 2-dpf embryos. Two clutches per group are shown; n = 30 (2 dpf) and n = 44 (3 dpf).

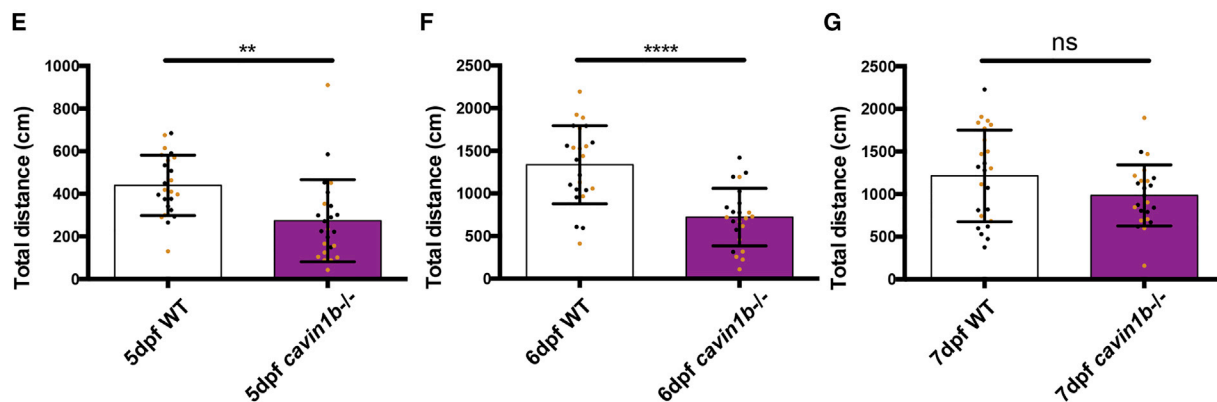
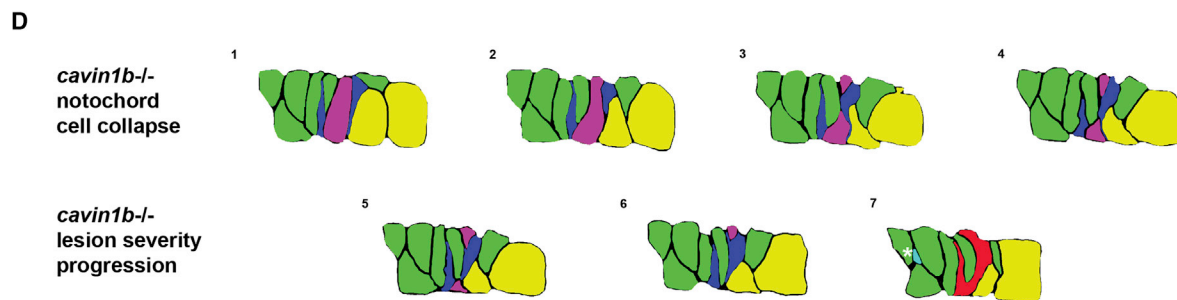
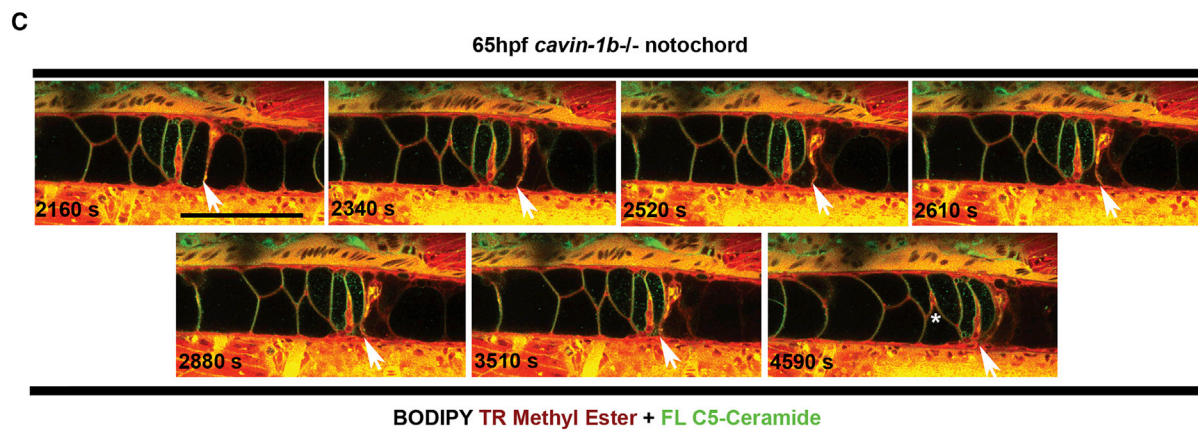
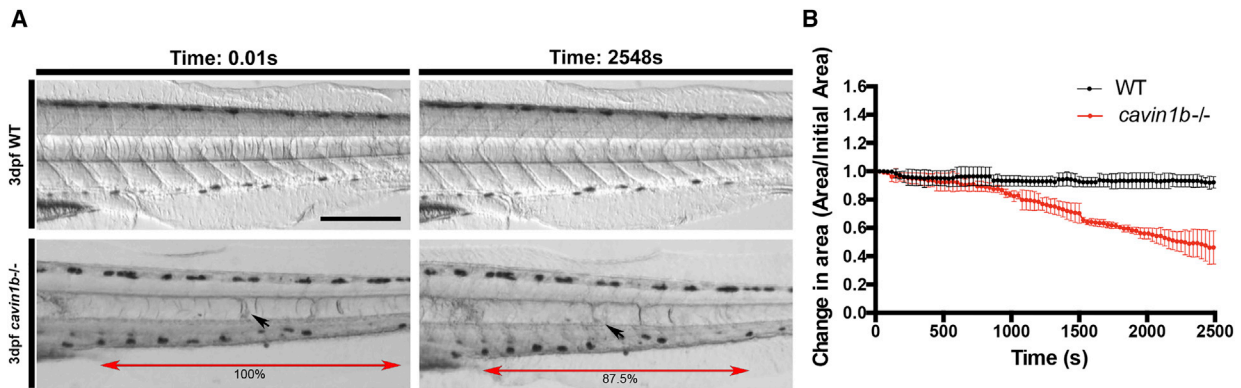
(C) Live image of a 4-dpf *cavin1b*^{-/-} embryo after electrical stimulation (10 min) at 3 dpf and corresponding unstimulated *cavin1b*^{-/-} control. Note that there are no skeletal muscle perturbations upon stimulation. The scale bar represents 1 mm. Images of WT controls after electrical stimulation are shown in Figure S6F. For the effects of electrical stimulation on the surface ultrastructure, see Figures S5A–S5D.

(D and E) Notochord lesion number (D) and severity index (E) for 3-dpf embryos and corresponding 4-dpf *cavin1b*^{-/-} embryos after electrical stimulation (10 min) at 3 dpf and corresponding unstimulated controls. ns, p > 0.05; ****p ≤ 0.0001; two-way ANOVA with Tukey's multiple-comparison test. Data are presented as mean ± SD; four clutches per group; n per group > 80. For proportion of notochord lesion severity, see Figure S6G. For a different mechanical loading experiment (chorion bleaching), see Figures S6B–S6E.

(F) Proportion of lesion severity in notochords of 3-dpf *cavin1b*^{-/-} embryos following anesthesia in tricaine (T) for 24 hr compared to 2- and 3-dpf unanesthetized *cavin1b*^{-/-} embryos. ****p ≤ 0.0001; chi square test.

(G and H) Lesion number (G) and severity index (H) in 3-dpf *cavin1b*^{-/-} embryos following anesthesia in T for 24 hr compared to 2- and 3-dpf unanesthetized *cavin1b*^{-/-} embryos. ns, p > 0.05; *p ≤ 0.05; ****p ≤ 0.0001; one-way ANOVA with Tukey's multiple-comparison test. Data are presented as mean ± SD.

For (F)–(H), n per group = 93 (2 dpf), 144 (3 dpf), and 83 (3 dpf with tricaine). Three clutches per group are shown. For tricaine washout experiments, refer to Figures S7A and S7B.



(legend on next page)

to the capacity of cells to build up or sustain high levels of membrane tension.

In summary, we have demonstrated a mechanoprotective, structural role for notochord caveolae in the early zebrafish embryo, in which an appropriate number of morphological caveolae is critical to protect notochord cells against tension experienced during swimming. The notochord evolved around 500 million years ago, resulting in the genesis of the chordate phylum and an entirely new form of locomotion [28, 42]. In light of our data, and because Cavin proteins (and indeed caveolae) have, to date, only been described in vertebrates [43], it seems likely that evolution of the cavin/caveolar system was necessary for the development of a stable notochord and consequently for the evolution of chordates.

STAR★METHODS

Detailed methods are provided in the online version of this paper and include the following:

- KEY RESOURCES TABLE
- CONTACT FOR REAGENT AND RESOURCE SHARING
- EXPERIMENTAL MODEL AND SUBJECT DETAILS
 - Zebrafish (*Danio rerio*)
- METHOD DETAILS
 - Animal handling and reagents
 - CRISPR/Cas9 generation of *cavin1b* mutants
 - Two-step reverse transcriptase (RT) PCR
 - Two-step qRT-PCR
 - Live imaging
 - Morphometrics of live zebrafish
 - Lesion qualification and quantification
 - High magnification live imaging
 - Notochord vacuole size and number measurement
 - Latrunculin treatment of embryos
 - Whole mount phalloidin staining
 - Live zebrafish notochord cell laser ablation
 - Intravenous microinjection of embryos
 - Mechanical stimulation of embryos
 - Tricaine treatment of embryos
 - Behavioral analysis of zebrafish

- Touch-evoked response assay
- Calcein staining of larvae
- Electron microscopy of zebrafish notochord
- Quantitation of caveola number and shape
- QUANTIFICATION AND STATISTICAL ANALYSIS

SUPPLEMENTAL INFORMATION

Supplemental Information includes seven figures, one table, and one movie and can be found with this article online at <http://dx.doi.org/10.1016/j.cub.2017.05.067>.

AUTHOR CONTRIBUTIONS

Conceptualization, Y.-W.L., H.P.L., T.E.H., G.A.G., J.G., and R.G.P.; Methodology, Y.-W.L., H.P.L., T.E.H., G.A.G., J.G., A.S.Y., and R.G.P.; Validation, Y.-W.L., T.E.H., and H.P.L.; Formal Analysis, Y.-W.L., J.G., G.A.G., N.M., and R.G.P.; Investigation, Y.-W.L., H.P.L., C.F., J.G., G.A.G., N.M., and R.G.P.; Writing – Original Draft, Y.-W.L., H.P.L., T.E.H., and R.G.P.; Writing – Review and Editing, Y.-W.L., H.P.L., T.E.H., J.G., G.A.G., C.F., A.S.Y., and R.G.P.; Visualization, Y.-W.L., H.P.L., G.A.G., T.E.H., and R.G.P.; Supervision, Y.-W.L., G.A.G., H.P.L., T.E.H., R.G.P., and A.S.Y.; Project Administration, H.P.L. and R.G.P.; Funding Acquisition, T.E.H., R.G.P., and A.S.Y.

ACKNOWLEDGMENTS

We thank the labs of Ben Hogan and Kelly Smith for their help with the CRISPR/Cas9 system setup. We thank Susan Nixon for designing *cavin1b* and *cav1* qRT-PCR primers. This work was supported by fellowships and grants from the National Health and Medical Research Council of Australia (to R.G.P., grant numbers 569542 and 1045092; to R.G.P. and A.S.Y., grant number APP1037320; to A.S.Y., grant number APP1044041; and to T.E.H. and R.G.P., grant number APP1099251) as well as by the Australian Research Council Centre of Excellence in Convergent Bio-Nano Science and Technology (to R.G.P., grant number CE140100036). Confocal microscopy was performed at the Australian Cancer Research Foundation (ACRF)/Institute for Molecular Bioscience (IMB) Dynamic Imaging Facility for Cancer Biology, established with funding from the ACRF. The authors acknowledge the facilities, and the scientific and technical assistance, of the Australian Microscopy & Microanalysis Research Facility at the Centre for Microscopy and Microanalysis, The University of Queensland.

Received: January 26, 2017

Revised: April 28, 2017

Accepted: May 22, 2017

Published: June 22, 2017

Figure 7. Live Imaging of *cavin1b*^{-/-} Notochord Cell Collapse from Prolonged Electrical Stimulation

(A) Video image stills of live 3-dpf *cavin1b*^{-/-} and WT embryos before and after prolonged electrical stimulation (~40 min). Note the change in morphology of a lesion (arrow) and the shortening of the body axis of the *cavin1b*^{-/-} embryo (red double-headed arrow indicates distance between two pigment cells is reduced by 12.5%). The scale bar represents 100 μ m.

(B) Change in notochord area spanning six somites under prolonged electrical stimulation (~40 min). Change in area is expressed as a ratio of initial area. Time interval = 30 s. Clutch size and n per group = 3. Data are presented as mean \pm SD.

(C) Live confocal time-lapse images of a 65-hpf *cavin1b*^{-/-} notochord colabeled with BODIPY TR methyl ester (endomembranes) and BODIPY FL C5-Ceramide (plasma membrane) under prolonged electrical stimulation (~76 min). Frame rate = 90 s; time stamp expressed in seconds. White arrow indicates a collapsing notochord cell region. A white asterisk marks the emergence of a new lesion between neighboring notochord cell borders. The scale bar represents 100 μ m. For corresponding WT control, see Figure S6H. See also Movie S1.

(D) Traces of confocal image sequences depicted in (C). Notochord cell membranes are traced. Prolonged electrical stimulation induces cellular collapse (purple-shaded cell), leaving behind membranous debris. Neighboring cells (shaded green) change shape to accommodate these morphological changes (prominent shape changes highlighted in yellow-shaded cells). During this sequence, two moderate lesions (dark blue shading) progress to form a single severe lesion (red shading). Concomitantly, a new mild lesion (light blue shading and highlighted by a white asterisk, *) appears distal to the existing lesion.

(E–G) Total spontaneous swimming distance covered by 5- (E), 6- (F), and 7-dpf (G) WT and *cavin1b*^{-/-} zebrafish over 1 hr (the same zebrafish were used for each time point). Colored dots indicate different clutches. For both lines, two clutches and n = 24 per group. ns, p > 0.05; **p \leq 0.01; ****p \leq 0.0001; two-tailed t test. Data are presented as mean \pm SD. See Figures S7C and S7D for touch-evoked response assay.

REFERENCES

1. Stemple, D.L. (2005). Structure and function of the notochord: an essential organ for chordate development. *Development* *132*, 2503–2512.
2. Ellis, K., Bagwell, J., and Bagnat, M. (2013). Notochord vacuoles are lysosome-related organelles that function in axis and spine morphogenesis. *J. Cell Biol.* *200*, 667–679.
3. Yamamoto, M., Morita, R., Mizoguchi, T., Matsuo, H., Isoda, M., Ishitani, T., Chitnis, A.B., Matsumoto, K., Crump, J.G., Hozumi, K., et al. (2010). Mib-Jag1-Notch signalling regulates patterning and structural roles of the notochord by controlling cell-fate decisions. *Development* *137*, 2527–2537.
4. Koehl, M.A.R., Quillin, K.J., and Pell, C.A. (2000). Mechanical design of fiber-wound hydraulic skeletons: the stiffening and straightening of embryonic notochords. *Am. Zool.* *40*, 28–41.
5. Adams, D.S., Keller, R., and Koehl, M.A. (1990). The mechanics of notochord elongation, straightening and stiffening in the embryo of *Xenopus laevis*. *Development* *110*, 115–130.
6. den Dunnen, J.T., and Antonarakis, S.E. (2000). Mutation nomenclature extensions and suggestions to describe complex mutations: a discussion. *Hum. Mutat.* *15*, 7–12.
7. Nixon, S.J., Carter, A., Wegner, J., Ferguson, C., Floetenmeyer, M., Riches, J., Key, B., Westerfield, M., and Parton, R.G. (2007). Caveolin-1 is required for lateral line neuromast and notochord development. *J. Cell Sci.* *120*, 2151–2161.
8. Hill, M.M., Bastiani, M., Luetterforst, R., Kirkham, M., Kirkham, A., Nixon, S.J., Walsler, P., Abankwa, D., Oorschot, V.M., Martin, S., et al. (2008). PTRF-Cavin, a conserved cytoplasmic protein required for caveola formation and function. *Cell* *132*, 113–124.
9. Nixon, S.J., Wegner, J., Ferguson, C., Méry, P.F., Hancock, J.F., Currie, P.D., Key, B., Westerfield, M., and Parton, R.G. (2005). Zebrafish as a model for caveolin-associated muscle disease; caveolin-3 is required for myofibril organization and muscle cell patterning. *Hum. Mol. Genet.* *14*, 1727–1743.
10. Smolders, L.A., Meij, B.P., Onis, D., Riemers, F.M., Bergknot, N., Wubbolts, R., Grinwis, G.C., Houweling, M., Groot Koerkamp, M.J., van Leenen, D., et al. (2013). Gene expression profiling of early intervertebral disc degeneration reveals a down-regulation of canonical Wnt signaling and caveolin-1 expression: implications for development of regenerative strategies. *Arthritis Res. Ther.* *15*, R23.
11. Lo, H.P., Nixon, S.J., Hall, T.E., Cowling, B.S., Ferguson, C., Morgan, G.P., Schieber, N.L., Fernandez-Rojo, M.A., Bastiani, M., Floetenmeyer, M., et al. (2015). The caveolin-cavin system plays a conserved and critical role in mechanoprotection of skeletal muscle. *J. Cell Biol.* *210*, 833–849.
12. Cheng, J.P., Mendoza-Topaz, C., Howard, G., Chadwick, J., Shvets, E., Cowburn, A.S., Dunmore, B.J., Crosby, A., Morrell, N.W., and Nichols, B.J. (2015). Caveolae protect endothelial cells from membrane rupture during increased cardiac output. *J. Cell Biol.* *211*, 53–61.
13. Kovtun, O., Tillu, V.A., Jung, W., Leneva, N., Ariotti, N., Chaudhary, N., Mandyam, R.A., Ferguson, C., Morgan, G.P., Johnston, W.A., et al. (2014). Structural insights into the organization of the cavin membrane coat complex. *Dev. Cell* *31*, 405–419.
14. Conti, E., and Izaurralde, E. (2005). Nonsense-mediated mRNA decay: molecular insights and mechanistic variations across species. *Curr. Opin. Cell Biol.* *17*, 316–325.
15. Esterberg, R., Delalande, J.M., and Fritz, A. (2008). Tailbud-derived Bmp4 drives proliferation and inhibits maturation of zebrafish chordamesoderm. *Development* *135*, 3891–3901.
16. Glickman, N.S., Kimmel, C.B., Jones, M.A., and Adams, R.J. (2003). Shaping the zebrafish notochord. *Development* *130*, 873–887.
17. Matsuda, R., Nishikawa, A., and Tanaka, H. (1995). Visualization of dystrophic muscle fibers in mdx mouse by vital staining with Evans blue: evidence of apoptosis in dystrophin-deficient muscle. *J. Biochem.* *118*, 959–964.
18. Hall, T.E., Bryson-Richardson, R.J., Berger, S., Jacoby, A.S., Cole, N.J., Hollway, G.E., Berger, J., and Currie, P.D. (2007). The zebrafish candyfloss mutant implicates extracellular matrix adhesion failure in laminin alpha2-deficient congenital muscular dystrophy. *Proc. Natl. Acad. Sci. USA* *104*, 7092–7097.
19. De, B.K., and Friedberg, I. (1991). Effect of ionophore A23187 on the membrane permeability in mouse fibroblasts. *Biochem. Biophys. Res. Commun.* *178*, 830–841.
20. Hapuarachchige, S., Montañó, G., Ramesh, C., Rodríguez, D., Henson, L.H., Williams, C.C., Kadavakkollu, S., Johnson, D.L., Shuster, C.B., and Arterburn, J.B. (2011). Design and synthesis of a new class of membrane-permeable triazaborolopyridinium fluorescent probes. *J. Am. Chem. Soc.* *133*, 6780–6790.
21. Liang, X., Michael, M., and Gomez, G.A. (2016). Measurement of mechanical tension at cell-cell junctions using two-photon laser ablation. *Biol. Protoc.* *6*, e2068.
22. Müller, U.K., and van Leeuwen, J.L. (2004). Swimming of larval zebrafish: ontogeny of body waves and implications for locomotory development. *J. Exp. Biol.* *207*, 853–868.
23. Long, J.H. (1995). Morphology, mechanics, and locomotion: the relation between the notochord and swimming motions in sturgeon. *Environ. Biol. Fishes* *44*, 199–211.
24. Thorsen, D.H., Cassidy, J.J., and Hale, M.E. (2004). Swimming of larval zebrafish: fin-axis coordination and implications for function and neural control. *J. Exp. Biol.* *207*, 4175–4183.
25. Budick, S.A., and O'Malley, D.M. (2000). Locomotor repertoire of the larval zebrafish: swimming, turning and prey capture. *J. Exp. Biol.* *203*, 2565–2579.
26. Fiaz, A.W., Léon-Kloosterziel, K.M., Gort, G., Schulte-Merker, S., van Leeuwen, J.L., and Kranenbarg, S. (2012). Swim-training changes the spatio-temporal dynamics of skeletogenesis in zebrafish larvae (*Danio rerio*). *PLoS ONE* *7*, e34072.
27. Attili, S., and Hughes, S.M. (2014). Anaesthetic tricaine acts preferentially on neural voltage-gated sodium channels and fails to block directly evoked muscle contraction. *PLoS ONE* *9*, e103751.
28. Annona, G., Holland, N.D., and D'Aniello, S. (2015). Evolution of the notochord. *Evodevo* *6*, 30.
29. Jiang, D., and Smith, W.C. (2007). Ascidian notochord morphogenesis. *Dev. Dyn.* *236*, 1748–1757.
30. Sinha, B., Köster, D., Ruez, R., Gonnord, P., Bastiani, M., Abankwa, D., Stan, R.V., Butler-Browne, G., Védie, B., Johannes, L., et al. (2011). Cells respond to mechanical stress by rapid disassembly of caveolae. *Cell* *144*, 402–413.
31. Fleming, A., Keynes, R., and Tannahill, D. (2004). A central role for the notochord in vertebral patterning. *Development* *131*, 873–880.
32. Haga, Y., Dominique, V.J., 3rd, and Du, S.J. (2009). Analyzing notochord segmentation and intervertebral disc formation using the *twhh:gfp* transgenic zebrafish model. *Transgenic Res.* *18*, 669–683.
33. Bensimon-Brito, A., Carreira, J., Cancela, M.L., Huysseune, A., and Witten, P.E. (2012). Distinct patterns of notochord mineralization in zebrafish coincide with the localization of Osteocalcin isoform 1 during early vertebral centra formation. *BMC Dev. Biol.* *12*, 28.
34. Fontaine, E., Lentink, D., Kranenbarg, S., Müller, U.K., van Leeuwen, J.L., Barr, A.H., and Burdick, J.W. (2008). Automated visual tracking for studying the ontogeny of zebrafish swimming. *J. Exp. Biol.* *211*, 1305–1316.
35. Gray, R.S., Wilm, T.P., Smith, J., Bagnat, M., Dale, R.M., Topczewski, J., Johnson, S.L., and Solnica-Krezel, L. (2014). Loss of *col8a1a* function during zebrafish embryogenesis results in congenital vertebral malformations. *Dev. Biol.* *386*, 72–85.
36. Kovtun, O., Tillu, V.A., Ariotti, N., Parton, R.G., and Collins, B.M. (2015). Cavin family proteins and the assembly of caveolae. *J. Cell Sci.* *128*, 1269–1278.

37. Walsen, P.J., Ariotti, N., Howes, M., Ferguson, C., Webb, R., Schwudke, D., Leneva, N., Cho, K.J., Cooper, L., Rae, J., et al. (2012). Constitutive formation of caveolae in a bacterium. *Cell* *150*, 752–763.
38. Liu, L., Brown, D., McKee, M., Lebrasseur, N.K., Yang, D., Albrecht, K.H., Ravid, K., and Pilch, P.F. (2008). Deletion of Cavin/PTRF causes global loss of caveolae, dyslipidemia, and glucose intolerance. *Cell Metab.* *8*, 310–317.
39. Morén, B., Shah, C., Howes, M.T., Schieber, N.L., McMahon, H.T., Parton, R.G., Daumke, O., and Lundmark, R. (2012). EHD2 regulates caveolar dynamics via ATP-driven targeting and oligomerization. *Mol. Biol. Cell* *23*, 1316–1329.
40. Stoeber, M., Stoeck, I.K., Hänni, C., Bleck, C.K., Balistreri, G., and Helenius, A. (2012). Oligomers of the ATPase EHD2 confine caveolae to the plasma membrane through association with actin. *EMBO J.* *31*, 2350–2364.
41. Ariotti, N., Hall, T.E., Rae, J., Ferguson, C., McMahon, K.A., Martel, N., Webb, R.E., Webb, R.I., Teasdale, R.D., and Parton, R.G. (2015). Modular detection of GFP-labeled proteins for rapid screening by electron microscopy in cells and organisms. *Dev. Cell* *35*, 513–525.
42. Satoh, N., Rokhsar, D., and Nishikawa, T. (2014). Chordate evolution and the three-phylum system. *Proc. Biol. Sci.* *281*, 20141729.
43. Hansen, C.G., and Nichols, B.J. (2010). Exploring the caves: cavins, cavolins and caveolae. *Trends Cell Biol.* *20*, 177–186.
44. Westerfield, M. (2000). *The Zebrafish Book: A Guide for the Laboratory Use of Zebrafish (Danio rerio)*, Fourth Edition (University of Oregon Press).
45. Williams, R.J., Hall, T.E., Glattauer, V., White, J., Pasic, P.J., Sorensen, A.B., Waddington, L., McLean, K.M., Currie, P.D., and Hartley, P.G. (2011). The in vivo performance of an enzyme-assisted self-assembled peptide/protein hydrogel. *Biomaterials* *32*, 5304–5310.
46. Gagnon, J.A., Valen, E., Thyme, S.B., Huang, P., Akhmetova, L., Pauli, A., Montague, T.G., Zimmerman, S., Richter, C., and Schier, A.F. (2014). Efficient mutagenesis by Cas9 protein-mediated oligonucleotide insertion and large-scale assessment of single-guide RNAs. *PLoS ONE* *9*, e98186.
47. Schindelin, J., Arganda-Carreras, I., Frise, E., Kaynig, V., Longair, M., Pietzsch, T., Preibisch, S., Rueden, C., Saalfeld, S., Schmid, B., et al. (2012). Fiji: an open-source platform for biological-image analysis. *Nat. Methods* *9*, 676–682.
48. Montague, T.G., Cruz, J.M., Gagnon, J.A., Church, G.M., and Valen, E. (2014). CHOPCHOP: a CRISPR/Cas9 and TALEN web tool for genome editing. *Nucleic Acids Res.* *42*, W401–W407.
49. Liew, W.C., and Orbán, L. (2014). Zebrafish sex: a complicated affair. *Brief. Funct. Genomics* *13*, 172–187.
50. Wilson, J.M., Bunte, R.M., and Carty, A.J. (2009). Evaluation of rapid cooling and tricaine methanesulfonate (MS222) as methods of euthanasia in zebrafish (*Danio rerio*). *J. Am. Assoc. Lab. Anim. Sci.* *48*, 785–789.
51. Pearen, M.A., Eriksson, N.A., Fitzsimmons, R.L., Goode, J.M., Martel, N., Andrikopoulos, S., and Muscat, G.E. (2012). The nuclear receptor, Nor-1, markedly increases type II oxidative muscle fibers and resistance to fatigue. *Mol. Endocrinol.* *26*, 372–384.
52. McCloy, R.A., Rogers, S., Caldon, C.E., Lorca, T., Castro, A., and Burgess, A. (2014). Partial inhibition of Cdk1 in G2 phase overrides the SAC and decouples mitotic events. *Cell Cycle* *13*, 1400–1412.
53. Bassett, D.I., Bryson-Richardson, R.J., Daggett, D.F., Gautier, P., Keenan, D.G., and Currie, P.D. (2003). Dystrophin is required for the formation of stable muscle attachments in the zebrafish embryo. *Development* *130*, 5851–5860.
54. Laird, A.S., Mackovski, N., Rinkwitz, S., Becker, T.S., and Giacomotto, J. (2016). Tissue-specific models of spinal muscular atrophy confirm a critical role of SMN in motor neurons from embryonic to adult stages. *Hum. Mol. Genet.* *25*, 1728–1738.
55. Du, S.J., Frenkel, V., Kindschi, G., and Zohar, Y. (2001). Visualizing normal and defective bone development in zebrafish embryos using the fluorescent chromophore calcein. *Dev. Biol.* *238*, 239–246.
56. Deerinck, T.J., Bushong, E.A., Thor, A., and Ellisman, M.H. (2010). NCMIR methods for 3D EM: a new protocol for preparation of biological specimens for serial block face scanning electron microscopy. <https://www.ncmir.ucsd.edu/sbem-protocol/>.

STAR★METHODS

KEY RESOURCES TABLE

REAGENT or RESOURCE	SOURCE	IDENTIFIER
Chemicals, Peptides, and Recombinant Proteins		
E3 Media	[44]	N/A
Phenol Red	Sigma-Aldrich	Cat#P0290-100ML
Bovine Serum Albumin Fraction V	Sigma-Aldrich	Cat#10735078001
T4 DNA Polymerase	New England BioLabs	Cat#M0203S
Recombinant Cas9 with NLS	PNA Bio	Cat#CP01-50
Gelatin	Sigma-Aldrich	Cat#G7765
Proteinase K	Sigma-Aldrich	Cat#P2308
SYBR Green PCR Master Mix	ThermoFisher Scientific	Cat#4309155
<i>N</i> -Phenylthiourea	Sigma-Aldrich	Cat#P7629-25G
Ethyl 3-aminobenzoate methanesulfonate (tricaine)	Sigma-Aldrich	Cat#E10521-10G
Paraformaldehyde	Sigma-Aldrich	Cat#P6148
TWEEN 20	Sigma-Aldrich	Cat#P9416
Dimethyl sulfoxide	Sigma-Aldrich	Cat#D8418
Saponin	Sigma-Aldrich	Cat#S7900
Horse serum	ThermoFisher Scientific	Cat#16050130
HEPES	ThermoFisher Scientific	Cat#15630080
DTT	Sigma-Aldrich	Cat#D0632
NP-40	Sigma-Aldrich	Cat#NP40S-100ML
SuperScript III Reverse Transcriptase	ThermoFisher Scientific	Cat#18080093
BODIPY FL C5-Ceramide	ThermoFisher Scientific	Cat#D3521
CellTrace BODIPY TR Methyl Ester	ThermoFisher Scientific	Cat#C34556
Latrunculin A	Sigma-Aldrich	Cat#L5163-100UG
Alexa Fluor 594 Phalloidin	ThermoFisher Scientific	Cat#A12381
Evans Blue	Sigma-Aldrich	Cat#E2129-10G
ChromaTide Alexa Fluor 488 5-UTP	ThermoFisher Scientific	Cat#C11403
Calcein	Sigma-Aldrich	Cat#C0875-5G
Critical Commercial Assays		
QIAquick PCR Purification Kit	QIAGEN	Cat#28104
MEGAscript T7 Transcription Kit	ThermoFisher Scientific	Cat#AM1354
RNA Clean & Concentrator –5	Zymo Research	Cat#R1015
LightCycler 480 High Resolution Melting Master	Roche Molecular Systems	Cat#04909631001
MeltDoctor HRM Master Mix	ThermoFisher Scientific	Cat#4415440
RNeasy Mini Kit	QIAGEN	Cat#74106
Experimental Models: Organisms/Strains		
Zebrafish: <i>TAB</i>	University of Queensland (UQ) Biological Resources Aquatics	N/A
Zebrafish: <i>Tg(actb2:EGFP-CAAX)^{pc10}</i>	[45]	N/A
Zebrafish: <i>cavin1b</i> ^{−/−uq7rp}	This paper	N/A
Zebrafish: <i>cavin1b</i> ^{−/−uq8rp}	This paper	N/A
Oligonucleotides		
CRISPR <i>cavin1b</i> gene-specific oligo:TAATACGACTCACTATAGG AGGGTGGCGAGATGAATGGTTTTAGAGCTAGAAATAGCAAG	This paper	N/A
CRISPR constant oligo:AAAAGCACCGACTCGGTGCCACTTTTTCAAG TTGATAACGGACTAGCCTATTTAACTTGCTATTTCTAGCTCTAAAAC	[46]	N/A

(Continued on next page)

Continued

REAGENT or RESOURCE	SOURCE	IDENTIFIER
HRMA <i>cavin1b</i> forward: GAGAAAGAAGAGGCTGGGGA	This paper	N/A
HRMA <i>cavin1b</i> reverse: TTTTGTCAAGCAGCGTGAGG	This paper	N/A
Sequencing <i>cavin1b</i> forward: CCTCCCGTCTCTGATGATG	This paper	N/A
Sequencing <i>cavin1b</i> reverse: TTACGCACCTTCTCCAGCAT	This paper	N/A
RT-PCR <i>cavin1b</i> forward: TCCTGACCACACCATCTACG	This paper	N/A
RT-PCR <i>cavin1b</i> reverse: ATGATCTTCCACCAGCACCA	This paper	N/A
RT-PCR <i>actb2</i> forward: GTCCCTGTACGCCTCTGGCT	This paper	N/A
RT-PCR <i>actb2</i> reverse: GCCGGACTCATCGTACTCCT	This paper	N/A
RT-qPCR primers	This paper	Table S1
Software and Algorithms		
Fiji	[47]	https://fiji.sc
GraphPad Prism 6	GraphPad Software	https://graphpad.com
NIS Elements Version 4.20	Nikon Instruments	https://www.nikoninstruments.com/Products/Software
Carl Zeiss ZEN 2012 (black edition)	Carl Zeiss	https://www.zeiss.com/microscopy/int/downloads/zen.html
CHOPCHOP	[48]	http://chopchop.cbu.uib.no
Adobe Photoshop CS6	Adobe Systems	https://www.adobe.com/au/products/photoshop
Adobe Illustrator CS6	Adobe Systems	http://www.adobe.com/au/products/illustrator

CONTACT FOR REAGENT AND RESOURCE SHARING

Further information and requests for reagent and resources should be directed to and will be fulfilled by the Lead Contact, Rob Parton (r.parton@imb.uq.edu.au).

EXPERIMENTAL MODEL AND SUBJECT DETAILS

Zebrafish (*Danio rerio*)

Zebrafish were raised and maintained according to institutional guidelines (Techniplast recirculating system, 14-h light/10-h dark cycle, The University of Queensland, UQ). Adults (90 dpf above) were housed in 3 or 8 L tanks with flow at 28.5°C, late-larval to juvenile stage zebrafish (6 dpf to 45 dpf) were housed in 1 L tanks with flow at 28.5°C and embryos (up to 5 dpf) were housed in 8 cm Petri dishes in standard E3 media (5 mM NaCl, 0.17 mM KCl, 0.33 mM CaCl₂, 0.33 mM MgSO₄) [44] at 28.5°C (incubated in the dark). All experiments were approved by the University of Queensland (UQ) Animal Ethics committee. The following zebrafish strains were used in this study: wild-type (TAB), an AB/TU line generated in UQBR Aquatics (UQ Biological Resources), *cavin1b*^{-/-uq7rp} (this paper), *cavin1b*^{-/-uq8rp} (this paper) and *Tg(actb2:EGFP-CAAX)^{pc10}* [45]. The developmental stages of zebrafish used in experiments (up to 15 dpf) are prior to specific sex determination [49] and specifically stated in corresponding figure legends. All zebrafish used in experiments were healthy, not involved in previous procedures and drug or test naive.

METHOD DETAILS

Animal handling and reagents

Zebrafish embryos up to 7 dpf were raised and handled in standard E3 media during experimental periods (5mM NaCl, 0.17mM KCl, 0.33 mM CaCl₂, 0.33 mM MgSO₄). All post-embryonic zebrafish measurements were carried out between tanks of similar population densities and conditions. All reagents were obtained from Sigma-Aldrich unless otherwise specified.

CRISPR/Cas9 generation of *cavin1b* mutants

Target site with >50% G/C content and no predicted off-target site for zebrafish *cavin1b* (NCBI: NM_001114549.2, corresponding Uniprot: A6NA21) specific sgRNA was selected using the webtool CHOPCHOP [48]. The method for cloning-independent synthesis of sgRNA was adopted from Gagnon et al. using the *cavin1b* gene-specific (containing T7 promoter site, spacer region and overlap region) and constant oligonucleotides mentioned in the [Key Resources Table](#) [46]. *Cavin1b*-specific sgRNA was produced by incubating the gene-specific and constant oligonucleotides together in an annealing reaction via the following reaction program (in a Veriti

96-Well Thermal Cycler): 95°C for 5 min, 95°C to 85°C (–2°C/s) and 85°C to 25°C at (–0.1°C/s). Following, in a fill-in reaction, 10 mM dNTP, NEB buffer 2, 100x bovine serum albumin (BSA) and T4 DNA polymerase were added to the product of the annealing reaction and incubated for 20 min at 12°C. The resulting DNA template was purified using the QIAquick PCR Purification Kit and subsequently run on a 3% TBE agarose gel for product verification. Following, sgRNA was transcribed using the Ambion MEGAscript T7 Transcription Kit with TURBO DNase incubation (15 min, 37°C) and purified using Zymo Research RNA Clean & Concentrator Kit. Recombinant Cas9 protein containing a nuclear localization signal (PNA Bio Inc) was reconstituted to a solution of 1 mg/mL recombinant Cas9 protein in 20 mM HEPES, 150 mM KCl, 1% sucrose (pH 7.9) and 1 mM DTT. An injection mixture of 700–753 ng/μL Cas9 protein, 200–208 ng/μL sgRNA and 16% phenol red was prepared and incubated for 5 min at room temperature (RT) to allow for Cas9-sgRNA complex formation. *Cavin1b*-targeting Cas9-sgRNA was injected into the cytoplasm of the early one-cell stage WT embryos. Injection volumes were calibrated to approximately 600–800 pL of injection mixture per injection.

Founder rate and percentage of mutant allele in f1 progenies was determined via high resolution melt analysis (HRMA). In the DNA preparation step, for whole-embryo tissue collection, selected 48 hpf embryos were anesthetized by rapid cooling [50] and added into the digestion buffer (1 M KCl, 1 M MgCl₂, 1 M Tris pH 8.3, 10% NP-40, 10% Tween-20, 0.1% gelatine, 20 mg/mL Proteinase K). For juvenile or adult zebrafish tissue collection, selected zebrafish was anesthetized in ethyl 3-aminobenzoate methanesulfonate (tricaine) solution, before cutting an approximately 3 mm piece of the caudal fin with a sterile razor blade and placing the fin clip in digestion buffer. The mixture was incubated at 60°C for 1 hr before reaction termination at 95°C for 15 min. Two different HRMA-compatible platforms were used (Applied Biosystems ViiA 7 Real-Time PCR System, using the MeltDoctor HRM Master Mix, and Roche LightCycler 480 System, using the LightCycler 480 High Resolution Melting Master). HRMA primers are as follows; forward: 5'-GAGAAAGAAGAGGCTGGGGA–3' and reverse 5'-TTTTGTCAAGCAGCGTGAGG–3'. When using the LightCycler 480 System, the high resolution melt (HRM) step was initiated after a standard PCR amplification step. The HRM step consists of a denaturation step at 95°C, followed by an annealing step at 65°C. Melt data acquisition began at 65°C and ended at 97°C with 15 fluorescence readings per degree centigrade at a 0.07°C/s ramp rate. When using the ViiA 7 Real-Time PCR System, the HRM step consists of a denaturation step at 95°C, followed by an annealing step at 60°C. Melt data acquisition began at 60°C and ended at 95°C at a 0.025°C/s ramp rate. Stable *cavin1b* f1 mutant zebrafish lines were confirmed using Sanger sequencing with the following primers: forward: 5'-CCTCCCGGTCTCTGATGATG–3' and reverse: 5'-TTACGCACCTTCTCCAGCAT–3'. Selected *cavin1b*^{–/–uq7rp} and *cavin1b*^{–/–uq8rp} lines were then bred to homozygosity. The *cavin1b*^{–/–uq7rp} line was also maintained on the *Tg(actb2:EGFP-CAAX)pc10* transgenic background [45].

Two-step reverse transcriptase (RT) PCR

RNA was isolated from zebrafish embryos (> 100 embryos randomly selected from 1 clutch) using the RNeasy Mini Kit (QIAGEN) and cDNA synthesis was performed using SuperscriptIII reverse transcriptase (ThermoFisher Scientific) as per the manufacturer's instructions. Amplifications were performed according to Hill et al. [8]. Primers used for amplification detailed in Table S1. Amplified products were separated and viewed via gel electrophoreses using 2% TAE agarose gels.

Two-step qRT-PCR

RNA isolation and cDNA synthesis was performed as described above for 5 dpf *cavin1b*^{–/–} and WT zebrafish embryos. qRT-PCR was performed using the SYBR Green PCR Master Mix on a ViiA7 Real-time PCR system (ThermoFisher Scientific) according to the manufacturer's instructions with three biological replicates (embryos randomly selected from 3 clutches) and three technical replicates on 96-well plates. qRT-PCR primers are listed in Table S1. Gene expression was analyzed using the ΔΔCt method [51]. Differences in expression were calculated using a two-way ANOVA with a posthoc Tukey's multiple comparison test.

Live imaging

For quantitating and qualifying notochord lesions, real-time observation of lesion formation and measurement of general embryonic morphology, embryos were incubated in 0.2 mM phenylthiourea (PTU) solution in E3 media to maintain embryo transparency for ease of notochord lesion visualization. Zebrafish (up to 15 dpf) were anesthetized in tricaine solution in E3, mounted in 1% low melting point (LMP) agarose in tricaine solution in a lateral view unless otherwise stated (anterior left, posterior right) and imaged using a Nikon SMZ1500 fluorescence stereomicroscope.

For early-stage 12 dpf larvae, zebrafish were anesthetized in tricaine and mounted in 1% LMP agarose in tricaine solution and imaged using the EVOS FL inverted fluorescence microscope (AMG).

Morphometrics of live zebrafish

Captured images using the NIS Elements Version 4.20 software via live imaging of zebrafish as described above were used to measure notochord diameter (at a constant area at the tip of the embryonic yolk extension) and body length (defined as the region from the tip of the anterior end of the zebrafish to the end of the trunk before the caudal fin). Measurements were non-blind and embryos were randomly selected from 2–4 biological replicates (clutches) with no prior formal sample-size estimation. Measurements were conducted using Fiji. Statistical analysis was carried out using two-tailed unpaired t tests.

Lesion qualification and quantification

In qualifying notochord lesions, three qualities of severity are identified via brightfield imaging using the Nikon SMZ1500 fluorescence stereomicroscope at x90 magnification, with embryos orientated at a constant position (anterior to the left). Mild lesions appear slightly delaminated with less apposed neighboring notochordal cells. Moderate lesions appear as lesions with larger delamination and are occasionally flanked by a small amount of fragmented vacuoles. Severe lesions appear as dense cellular regions with a larger delamination compared to moderate lesions, and are flanked by, and/or consist of small fragmented vacuoles. These lesions are represented in Figure 1H.

In quantitating notochord lesions, the notochord of a live zebrafish embryo was viewed at x90 magnification via live imaging of zebrafish as described above. The number of lesions in one particular notochord is recorded in Microsoft Excel and the qualities of severity of each lesion were recorded in the same Microsoft Excel spreadsheet using a severity index describing mild, moderate and severe lesions with the arbitrary values of 2, 3 and 4 respectively. The severity index score was calculated by adding the arbitrary values of mild (2), moderate (3) and severe (4) and taking the sum of values for each individual notochord. The arbitrary values are approximations of relative lesion site size and degree of fragmentation in vacuoles. Embryos used for measurements of lesion number and severity index score in relevant experiments were randomly selected from 2-4 biological replicates (clutches) with no prior formal sample-size estimation. Measurements were non-blind. Statistical analyses were carried out using two-tailed unpaired t tests, ordinary one-way ANOVA with posthoc Tukey's multiple-comparison tests or two-way ANOVA with posthoc Tukey's multiple-comparison tests. The proportion of lesion severity was calculated by taking the proportions of the total number of mild, moderate and severe lesions counted and expressing the values as proportion percentages in a total number of embryos. Embryos used for measurements of proportion of lesion severity in relevant experiments were randomly selected from 3-4 biological replicates (clutches) with no prior formal sample-size estimation. Measurements were non-blind. Statistical analyses were carried out using chi square tests.

High magnification live imaging

For high magnification and resolution imaging and live timelapse of notochord lesions, zebrafish embryos were incubated at 28°C in either or both BODIPY FL C5-Ceramide and BODIPY TR methyl ester (ThermoFisher Scientific) for 24 and/or 2 hr respectively, anesthetized in tricaine, mounted in 1% LMP agarose in tricaine solution and imaged using a Zeiss LSM 710 upright confocal microscope equipped with a x40/1.0 W N-Achroplan M27 water immersion lens.

Notochord vacuole size and number measurement

Captured images using the Zeiss LSM 710 upright confocal microscope on the Carl Zeiss ZEN 2012 (black edition) software via the high magnification live imaging of zebrafish technique as described above were used to measure individual vacuole size in Fiji. The embryos were labeled using BODIPY TR methyl ester and imaged in a dorsal view (frontal plane) at the anterior end of the yolk extension (avoiding the imaging of notochord areas containing lesions). Images containing notochord lesions were excluded from measurements. Embryos used for measurements were randomly selected from 4 biological replicates (clutches) with no prior formal sample-size estimation. Measurements were non-blind. Statistical analyses were carried out using two-tailed unpaired t tests

Latrunculin treatment of embryos

Live *cavin1b*^{-/-} or WT zebrafish were treated with 1.25 μM Latrunculin A in E3 media (Sigma-Aldrich) for 35 min and subsequently washed 4 times in E3 media.

Whole mount phalloidin staining

Our staining protocol was modified from previous publication [9]. Zebrafish were anesthetized using tricaine and fixed in 4% paraformaldehyde overnight. The embryos were washed into methanol and incubated overnight at -20°C. The embryos were then washed into PBS/0.1% Tween-20 (PBST) and blocked in a blocking solution (1% BSA, 1% DMSO, 0.2% saponin and 1% horse serum) for 2 hr at RT. The embryos were then incubated in Alexa Fluor 594 Phalloidin (ThermoFisher Scientific) in 1:20 dilution overnight at 4°C and washed in the blocking solution over the course of 2 hr. Following, the embryos were washed into PBST, then PBS, and stored at 4°C. For imaging, stained embryos were mounted in 1% LMP agarose in PBS and imaged using a Zeiss LSM 710 upright confocal microscope equipped with a x40/1.0 W N-Achroplan M27 water immersion lens.

Stained embryos were imaged and captured from a dorsal view (frontal plane) at the anterior end of the yolk extension as described above and images were analyzed using Fiji. To measure corrected total fluorescence, the integrated density of the imaged notochords were measured and subtracted with the mean of background mean gray value of 3 randomly selected vacuoles x the area of the imaged notochord as modified from previous publications [52]. Images containing notochord lesions were excluded from measurements. Embryos used for measurements were randomly selected from 2-3 biological replicates (clutches) with no prior formal sample-size estimation. Measurements were non-blind. Statistical analyses were carried out using a two-tailed unpaired t test and an ordinary one-way ANOVA with posthoc Tukey's multiple-comparison test.

Live zebrafish notochord cell laser ablation

Live 2 dpf *cavin1b*^{-/-} or WT zebrafish expressing EGFP-CAAX were anesthetized and mounted in 1% LMP agarose on MatTek glass bottom dishes with a dorsal view (frontal plane) and imaged using the LSM 710 Meta inverted confocal microscope equipped with a

multiphoton Mai Tai eHP 760-1040nm laser. Laser ablation was carried out as previously described under the 40x, 1.3 NA Plan Apochromat oil immersion objective at 28°C [21] with modifications. 3-5 ablation sites were randomly selected along the length of the yolk extension and a time series of approximately 8 s (time interval 0.95 s) was performed post ablation. Notochords containing lesions were excluded from the experiment. Data analysis of recoil measurements after laser ablation, instantaneous recoil velocity at time = 0 and K value was performed as previously published [21]. Briefly, the MTrackJ plugin from Fiji was used to analyze the time-lapse images after application of a median filter (1 pixel). The strain or deformation $\epsilon(t)$ of the notochord cell-cell junction was measured as a function of time after ablation by tracking the XY coordinates of each vertex resulting from the ablated junction over time and data was collected in Microsoft Excel. The length of the contact $L(t)$ for each time point was calculated using the following formula: $L(t) = \sqrt{((X_{\text{top}}(t) - X_{\text{bottom}}(t))^2 + (Y_{\text{top}}(t) - Y_{\text{bottom}}(t))^2)}$. The amount of strain [$\epsilon(t)$] after ablation is then measured using the following formula: $\epsilon(t) = L(t) - L(0)$. Fitting of the data was acquired using the following equation: $\epsilon(t) = L(t) - L(0) = F_0/E \cdot (1 - e^{-((E/\mu) \cdot t)})$ where F_0 is the tensile force present at the junction before ablation, E is junction elasticity and μ is viscosity coefficient related to the viscous drag of the cell cytoplasm. We utilized the following equations; initial recoil = $d\epsilon(0)dt/dt = F_0/\mu$ and K value = E/μ as fitting parameters. Fitting of the recoil data was carried out using GraphPad PRISM. Embryos used for measurements were randomly selected from 2 biological replicates (clutches) with no prior formal sample-size estimation. Measurements were non-blind. Statistical analyses were carried out using two-tailed unpaired t tests.

Intravenous microinjection of embryos

For Evans Blue dye injection (EBD), pericardial injection of approximately 5 nL of 0.1 mg/mL EBD via the common cardinal vein was performed on zebrafish embryos as previously described [53]. Embryos were incubated at 28°C for 3 hr to ensure sufficient EBD circulation and uptake. Anesthetized embryos were mounted and imaged as described in live imaging of zebrafish above. Embryos were randomly selected from 1 biological replicate (clutch).

For Alexa Fluor 488 5-UTP microinjections, zebrafish embryos were labeled with BODIPY TR methyl ester as described above, followed by a pericardial injection of approximately 5 nL of Alexa Fluor 488 5-UTP solution via the common cardinal vein. Embryos were incubated at 28°C for 2 hr to ensure sufficient fluorophore circulation and uptake. Anesthetized embryos were mounted and imaged as described in high magnification live imaging of zebrafish above. Embryos were randomly selected from 1 biological replicate (clutch).

Mechanical stimulation of embryos

For bleaching experiments, 1 dpf zebrafish embryos were incubated in a mild bleaching solution (40 μ L 10% sodium hypochlorite solution in 50 mL E3 media) for 10 min at RT. Embryos were then washed three times in E3 media and placed in 0.2 mM PTU solution until 112 hpf at 28°C. At 112 hpf, embryos were manually dechorionated and notochord lesion quantitation and qualification were performed as described above.

For electrical stimulation experiments, 3 dpf zebrafish embryos were first placed in 3.5 cm culture dishes, anesthetized in tricaine and notochord lesion quantitation and qualification were performed as above. Embryos were then washed three times in E3 media and subjected to electrical stimulation using a constant voltage electrical stimulator (Square Pulse Stimulator S44, Grass Instruments) with the following settings: stimulation rate: 4 pps x 0.1, delay: 9 ms x 0.1, duration: 9 ms x 0.1, voltage: 12 V x 10 for 10 min. Electrodes were manually circulated evenly around the culture dish to ensure even stimulation in all embryos. For unstimulated controls, electrodes connected to the stimulator with the power turned off were manually circulated evenly around the culture dish for 10 min. Zebrafish were then incubated at 28°C before notochord lesion quantitation and qualification repeated 24 hr post stimulation.

For prolonged electrical stimulation, 3 dpf zebrafish embryos were anesthetized in tricaine, mounted in 1% LMP agarose and subjected to electrical stimulation using a constant voltage electrical stimulator (Square Pulse Stimulator S44, Grass Instruments) with the following settings: stimulation rate: 4 pps x 0.1, delay: 9 ms x 0.1, duration: 8 ms x 0.1, voltage: 11.6 V x 1 for 40 min under a Nikon SMZ1500 fluorescence stereomicroscope at RT, or for approximately 76 min (see below). Video was taken using NIS Elements Version 4.20 AVI acquisition tool at 7 fps. Constant notochord area was determined by approximating a length of 6-somites from the anus of the zebrafish using Fiji. Embryos were randomly selected from 3 biological replicates (clutches).

For high resolution live timelapse of lesion formation, 65 hpf zebrafish embryos were anesthetized in tricaine, embedded in 1% LMP agarose and subjected to approximately 76 min of prolonged electrical stimulation with the same parameters above on a constant voltage electrical stimulator using electrodes mounted on a x40/1.0 W N-Achroplan M27 water immersion lens at RT. Timelapse was taken using a Zeiss LSM 710 upright confocal microscope on the Carl Zeiss ZEN 2012 (black edition) software.

For high intensity electrical stimulation, individual 3 dpf WT or *cavin1b*^{-/-} embryo was placed in a glass dish and electrically stimulated using an electrical stimulator (Square Pulse Stimulator S44, Grass Instruments) with the following settings: stimulation rate: 6 pps x 1, delay: 9 ms x 0.01, duration: 10 ms x 10, voltage: 5.5 V x 10 for 80 s. Five seconds before the end of stimulation, 2.5% glutaraldehyde in 2X PBS was added to the dish containing stimulated embryo in equal volume with the E3 media and placed for 3 min in a Pelco Biowave under vacuum and irradiated at 80 W. Electron microscopy was carried out as described below. Tricaine anesthetized embryos were used as a control.

Tricaine treatment of embryos

At 1 dpf, zebrafish embryos were dechorionated by incubation in 1 mg/mL pronase solution at RT for 5 min, then washed three times in E3 media. Embryos were anesthetized in a standard tricaine solution (0.16 mg/mL in E3 media) for up to 24 hr at 28°C in the

locomotion inhibition experiments. For tricaine washout experiments, during the washout step, embryo plates containing tricaine solution were rinsed and washed three times with fresh E3 media. Quantitation and qualification of notochord lesions were carried out as described above.

Behavioral analysis of zebrafish

Swimming behavioral analysis was carried out using the ZebraBox Revolution following manufacturer's instructions (<http://www.viewpoint.fr/en/p/equipment/zebrabox>) and as previously described [54]. One WT or *cavin1b*^{-/-} larva was placed in each well of 24-well plates filled with 1 mL of E3 media. The plates were incubated at 28°C in the dark prior to the experiments. Larva spontaneous swimming behaviors were recorded for 1 hr at RT under normal lighting condition and without specific stimulation. Time points of 5, 6 and 7 dpf were used (same zebrafish for each time point). At the end of the experiment, each larva was checked in order to exclude potential dead animals from the data. Data were exported and processed using Microsoft Excel to analyze and compare total distance traveled during the 1 hr recording period. Zebrafish used for measurements were randomly selected from 2 biological replicates (clutches) with no prior formal sample-size estimation. Measurements were non-blind. Statistical analyses were carried out using two-tailed unpaired t tests.

Touch-evoked response assay

4 and 5 dpf zebrafish embryos were placed in a petri dish filled with E3 media. From which, single embryos were placed in individual petri dish on a determined spot. Tactile stimuli were applied to the tail of the embryo with a pair of no. 5 forceps, up to 3 times. Only embryos that responded with straight swimming upon touch stimuli were recorded. Embryos that did not respond after 3 touch stimuli or exhibited turning behaviors after touch stimuli were not used for the experiment. Captured images were used to determine distance traveled in measures of body length. Embryos used for measurements were randomly selected from 3 biological replicates (clutches) with no prior formal sample-size estimation. Measurements were non-blind. Statistical analyses were carried out using two-tailed unpaired t tests.

Calcein staining of larvae

This protocol is adapted from Du et al. [55]. Zebrafish early-stage larvae were incubated in 0.2% calcein solution (pH 7.0) for 10 min and washed in aquarium system water three times. Anesthetized embryos were mounted in 1% LMP agarose and imaged as described above. Imaging was carried out using a Nikon SMZ1500 fluorescence stereomicroscope.

Electron microscopy of zebrafish notochord

This protocol is a modified version originally by Deerinck et al. [56], and designed to enhance membrane contrast using reduced osmium tetroxide, thiocarbohydrazide-osmium, uranyl acetate and en bloc lead nitrate staining. A solution containing 2.5% glutaraldehyde in 2X PBS was added to the dish in equal volume with anesthetized zebrafish embryos and placed for 5 min in a Pelco Biowave under vacuum and irradiated at 80 W. Embryos were reduced in size by removing the head and tail, and again irradiated in fresh fixative (2.5% glutaraldehyde), under vacuum, for a further 6 min. Embryos were washed 4 × 2 min in 0.1 M cacodylate buffer. A solution containing both potassium ferricyanide (1.5%) and osmium tetroxide (2%) in 0.1 M cacodylate buffer was prepared and samples immersed for 30 min at RT. Following 6 × 3 min washes in distilled water, samples were then incubated in a filtered solution containing thiocarbohydrazide (1%) for 30 min at RT. After subsequent washing in distilled water (6 × 2 min), samples were incubated in an aqueous solution of osmium tetroxide (2%) for 30 min. Samples were washed again in distilled water (6 × 2 min) and incubated in 1% uranyl acetate (aqueous) for 30 min at 4°C. Further distilled water washes (2 × 2 min) were completed before adding a freshly prepared filtered 0.06% lead nitrate in aspartic acid (pH 5.5) solution warmed to 60°C. The lead nitrate solution containing tissue blocks was further incubated for 20 min at 60°C before rinsing in distilled water (6 × 3 min) at RT. Samples were dehydrated twice in each ethanol solution of 30%, 50%, 70%, 90% and 100% absolute ethanol for 40 s at 250 W in the Pelco Biowave. Epon LX112 resin was used for embedding the tissue with infiltration steps at 25%, 50%, 75% resin to ethanol in the Pelco Biowave under vacuum at 250 W for 3 min and finishing with 100% resin (twice), before the final resin embedding and placed in a 60°C oven for 12 hr. Blocks were sectioned on a Leica UC64 ultramicrotome at 60 nm and mounted on formvar coated 3 slot Cu grids. Thin sections (60 nm) were viewed on a Jeol JEM-1011 at 80kV.

Quantitation of caveola number and shape

For caveola number: electron micrographs of the notochord plasma membrane septal regions were taken at random at a primary magnification of 50,000x from 3 dpf WT and *cavin1b*^{-/-} embryos. The number of caveolae, which is defined as 40-70 nm uncoated invaginations and vesicular profiles with 100 nm of the plasma membrane was counted and expressed as density per micron of linear length along the plasma membrane, independent of the invaginations. For caveola shape: using the same random electron micrographs as described above, uncoated invaginations were traced in Adobe Photoshop CS6 for 3 dpf WT and *cavin1b*^{-/-}. The neck and depth (from the top to the base) of the invaginations were measured and the ratio of neck to depth was used as an indicator of shape. Embryos used for measurements were randomly selected from 3 biological replicates (clutches) with no prior formal sample-size estimation. Measurements were non-blind. Statistical analyses were carried out using two-tailed unpaired t tests.

QUANTIFICATION AND STATISTICAL ANALYSIS

All image measurements and analyses were carried out using Fiji [47] unless otherwise stated. Statistical analysis, graphs and tables were produced using GraphPad Prism version 6.0 for Mac OS X, GraphPad Software, La Jolla California USA and Microsoft Excel 14.4.9. Figures were composed using Adobe Photoshop CS6 and Adobe Illustrator CS6.

Statistical details of experiments can be found in the figure legends, including the statistical tests used (two-tailed unpaired t tests for 2 groups, ordinary one-way ANOVA with a posthoc Tukey's multiple-comparison test for 3 or more groups, two-way ANOVA with a posthoc Tukey's multiple-comparison test for comparing 2 factors with multiple treatment groups) and n (represents number of zebrafish used unless otherwise stated in the figure legends). For data involving Tukey's multiple-comparison tests, multiplicity adjusted p value was reported for each comparison. Data are presented as mean \pm standard deviation. p values are summarized as the following: ns = $p > 0.05$; * $p \leq 0.05$; ** $p \leq 0.01$; *** $p \leq 0.001$; **** $p \leq 0.0001$.